
State and Force Estimation of a Point Absorber Wave Energy Converter

DIPLOMA THESIS

Conducted in partial fulfillment of the requirements for the degree of a
Diplom-Ingenieur (Dipl.-Ing.)

supervised by

Associate Prof. Dr.-Ing. Wolfgang Kemmetmüller
Dr. techn. Gabriel Forstner

submitted at the

TU Wien
Faculty of Electrical Engineering and Information Technology
Automation and Control Institute

by

Tobias Glaser
Matriculation number 1427786

Wien, January 2, 2024

Complex Dynamical Systems Group

A-1040 Wien, Gußhausstr. 27–29, Internet: <https://www.acin.tuwien.ac.at>

Preamble

First and foremost, I want to express my gratitude to Associate Prof. Dr.-Ing. Wolfgang Kemmetmüller for giving me the opportunity to conduct this thesis and for his valuable feedback and advices. I would also like to extend my thanks to my supervisor at CorPower Ocean, Dr.techn. Gabriel Forstner, for the insightful discussions, helpful inputs, and for granting me the opportunity to work on this thesis on-site in Stockholm for several months. I am very grateful for this time, the valuable exchange with my colleagues at CorPower Ocean and for sharing their knowledge and experience with me.

Further, I would like to thank Univ.-Prof. Dr.tech Andreas Kugi and the CDS team for their dedication to teaching and the interesting courses. These experiences have awakened my enthusiasm for control engineering and allowed me to significantly enhance and deepen my knowledge in this field.

A special thanks goes to my friend Manuel Deuerling, who was always at my side and supported and motivated me even in difficult times during my studies.

Finally, I would like to thank my parents and brothers for their support and encouragement during this time

Wien, January 2, 2024

Abstract

Wave energy is among the largest untapped resources of renewable energy. As waves have the highest energy density of all renewable energy sources, wave energy converters (WECs) have considerable potential to contribute to the global energy mix. However, for WECs to become a cost-effective alternative, effective control strategies are essential. Advanced control techniques rely on the excitation force of the wave as an input, which is not measurable. Therefore, accurate and reliable estimates are essential. Using the Euler-Lagrange equations, a simplified nonlinear dynamic model for a point absorber WEC is derived in this thesis. Numerical simulations demonstrate that the model captures the relevant dynamics of the WEC in three degrees of freedom. Based on this model, a state observer is designed that is able to provide estimates for the excitation force and the wave elevation. To increase the robustness of the estimation, several sensors are used. The performance of the observer is evaluated across various sea states using a comprehensive six-degree-of-freedom model. Various sensor failures are also simulated to determine the reliability of the observer. Further, the significance of using a three-degree-of-freedom model for estimation is shown.

Kurzzusammenfassung

Wellenenergie gilt als eine der größten ungenutzten erneuerbarer Energiequellen. Durch die hohe Energiedichte der Wellen haben Wellenenergiekonverter (WEC) ein erhebliches Potenzial einen bedeutenden Teil zum globalen Energiemix beizutragen. Damit WECs jedoch zu einer kosteneffizienten Alternative werden, sind effektive Regelungsstrategien unerlässlich. Fortgeschrittene Regelungsmethoden benötigen die Erregungskraft der Welle als Eingang, die aber nicht messbar ist. Daher sind akkurate und zuverlässige Schätzungen entscheidend. Unter Verwendung der Euler-Lagrange-Gleichungen wird in dieser Arbeit ein vereinfachtes nichtlineares dynamisches Modell für ein Punktabsorber-WEC hergeleitet. Anhand numerischer Simulationen wird gezeigt, dass das Modell die relevanten Dynamiken des WECs unter der Verwendung von drei Freiheitsgraden abbildet. Auf der Grundlage dieses Modells wird ein Zustandsbeobachter entworfen, der in der Lage ist, Schätzungen für die Erregungskraft und die Wellenhöhe zu liefern. Um die Robustheit der Schätzung zu erhöhen, werden mehrere Sensoren mit dem Zustandsbeobachter kombiniert. Die Performance des Beobachters wird anhand eines detaillierten Modells mit sechs Freiheitsgraden unter Berücksichtigung verschiedener Seegänge ermittelt. Außerdem werden verschiedene Sensorausfälle simuliert, um die Zuverlässigkeit des Beobachters zu bewerten. Die Bedeutung der Verwendung eines Modells im Beobachter, basierend auf drei Freiheitsgraden, wird zudem gezeigt.

Contents

1	Introduction	1
1.1	Point Absorber Wave Energy Converter	1
1.2	Literature Survey	2
1.2.1	Estimation based on 1DoF models	3
1.2.2	Estimation based on multi-DoF models	3
1.3	Goals of this Thesis	4
1.4	Content and Structure	4
2	Theory and Simulation Setup	6
2.1	Linear Wave Theory	6
2.2	Hydrodynamic and Hydrostatic Forces	7
2.2.1	Excitation Force	7
2.2.2	Radiation Force	8
2.2.3	Nonlinear Extension and Buoyancy Force	8
2.2.4	Drag Force	9
2.3	Wave-to-Wire Model	9
2.4	Sensors	10
3	Mathematical Modeling	12
3.1	WEC Model	12
3.1.1	Assumptions and Notations	12
3.1.2	Kinematics	14
3.1.3	Dynamics	17
3.1.4	External Forces	18
3.1.5	Model Simplification	22
3.2	Oscillator Model	24
3.3	Sensor Models	25
3.3.1	Encoder	25
3.3.2	Pressure Sensor	25
3.3.3	Inertial Measurement Unit	26
4	Estimation	28
4.1	Dynamic System	28
4.2	Extended Kalman Filter	29
4.3	Tuning	30
4.3.1	Measurement Noise	30
4.3.2	Process Noise	31
4.3.3	Initial Error Covariance	32

4.4	Results	32
4.4.1	Assessment of EKF and Bias Compensation	33
4.4.2	Comparison of EKF and Linear KF	37
4.4.3	Robustness against Sensor Failures	42
4.4.4	Impact of Degrees of Freedom	44
5	Conclusion and Outlook	46

List of Figures

1.1	CorPower Ocean C4 wave energy converter [7].	2
2.1	Probability of sea states for Agucadoura (%) [46]	10
2.2	Location of the sensors [7]	11
3.1	Schematic representation of the WEC	13
3.2	Kinematic model of WEC: a) coordinate frames according to DH convention b) used coordinate frames for model	15
3.3	Machinery force components acting on the buoy	21
3.4	Open loop model comparison under irregular sea state ($H_s = 1.75\text{m}$, $T_e = 7\text{s}$).	23
4.1	Tuning of process noise variance for the harmonic oscillator states	32
4.2	Estimated wave elevation of EKF without pressure measurement ($H_s = 1.75\text{m}$, $T_e = 10\text{s}$).	33
4.3	Impact of η_0 on the distribution of the estimation errors without pressure sensor	35
4.4	Impact of η_0 on the distribution of the estimation errors with pressure sensor	36
4.5	Magnitude response of $H_p(\omega)$	37
4.6	Time series comparison ($H_s = 1.75\text{m}$, $T_e = 7\text{s}$).	38
4.7	Comparison of the distribution of the estimation errors	41
4.8	Boxplot comparison of the accuracy of the linear KF and the EKF	42
4.9	Robustness of EKF against single sensor failures	43
4.10	Robustness of EKF against multiple sensor failures	44
4.11	Impact of degrees of freedom considered in estimation ($H_s = 1.75\text{m}$, $T_e = 7\text{s}$).	45

List of Tables

3.1	Denavit-Hartenberg parameters	14
4.1	NRMSA comparison of observers for sea states in tuned mode	40

1 Introduction

The first attempts to harness energy from ocean waves date back to 1799 [1], but the increasing effects of global warming and technological progress, for example, have reignited interest in wave energy. Its high energy density, availability, and predictability make it a powerful and attractive renewable energy source [2]. Although there are multiple ways of harnessing wave energy, the main idea relies on capturing the movement of sea waves and converting it into other forms of energy, mostly electricity. However, the irregular behavior of ocean waves poses a challenge for the optimal control of such devices, called wave energy converters (WECs). Usually, the estimation and prediction of significant quantities, such as the wave elevation of the incident wave or the force caused by it on the WEC (known as the excitation force) are required [3]. Before the motivation and goals of this thesis are discussed in more detail, a description of the WEC considered in this work is provided, followed by a literature review.

1.1 Point Absorber Wave Energy Converter

The WEC considered in this work is the C4 wave energy converter from CorPower Ocean [4]. The C4 operates as a point absorber wave energy converter, meaning that the wave's energy is harnessed through the relative motion between a moving body and a stationary structure. In Figure 1.1, the moving body is represented by the buoy, oscillating in response to waves. The WEC is attached to the seabed by the mooring rod and the anchor, providing the stationary reference. The mooring rod and anchor are linked through a universal joint, allowing the WEC to be deflected laterally by incoming waves. Furthermore, the mooring rod contains the tidal regulator, enabling the WEC to adapt to changing tides. The buoy can move along the ocean rods that connect the mooring rod to the stationary part inside the buoy. The most relevant components inside the buoy are shown in Figure 1.1. The pretension cylinder and the so-called WaveSpring [4, 5], are both pressure cylinders. The pretension cylinder is used to set the initial position of the buoy, while the WaveSpring acts as a negative spring that amplifies the motion of the buoy and increases the power absorption of the system [5]. The rack, which moves together with the buoy, enters the gearbox, where the linear motion transforms into rotary motion, subsequently captured by the generators and converted into electrical energy. This conversion from mechanical to electrical energy via the generators is commonly referred to in the literature as the power take-Off (PTO) system [6].

The main control objective is to maximize energy absorption by the PTO. As shown in [8], the optimal control problem is in general non-causal, which either requires forecasting techniques, usually for the excitation force, or a causal approximation. In addition, physical constraints on position, velocity and control inputs must commonly be respected

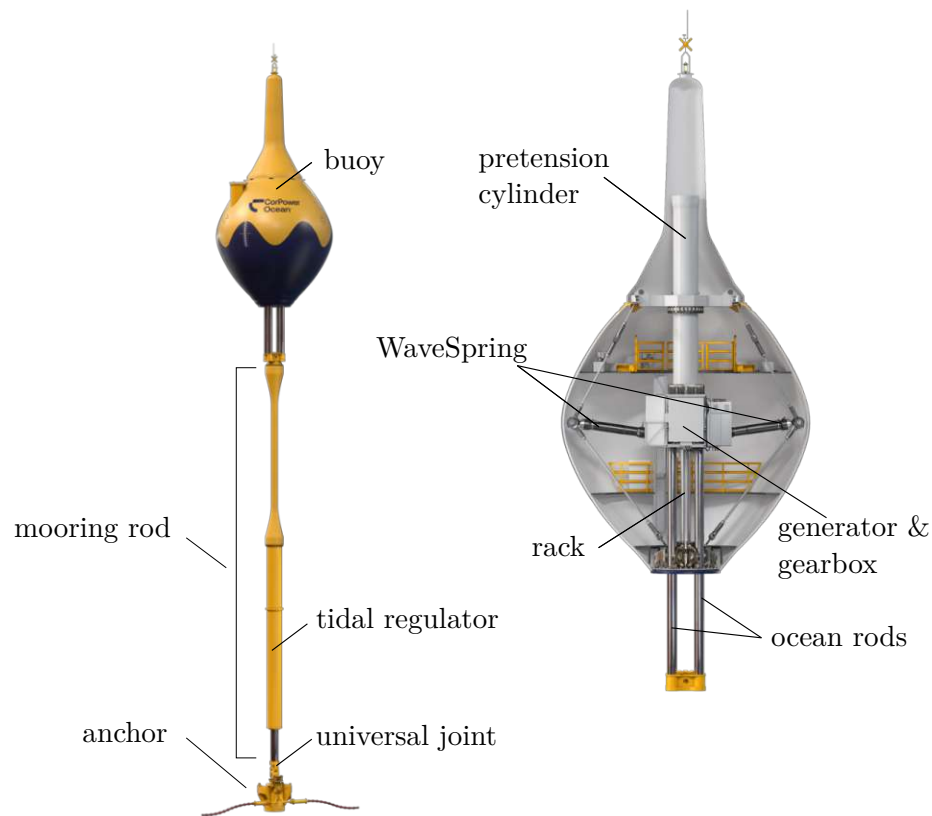


Figure 1.1: CorPower Ocean C4 wave energy converter [7].

by the controller. Due to these requirements, the use of model predictive control (MPC) for WECs has gained popularity as an alternative to conventional control strategies [8]. MPC-based control algorithms still require future knowledge of the excitation force. As this quantity is immeasurable, it needs to be estimated in first place, which makes its estimation become a crucial part in optimal control.

1.2 Literature Survey

In recent years, considerable research has focused on estimating the excitation force and different estimation strategies have been proposed in the literature. In the strategies presented in [9, 10], the excitation force is simply calculated from wave elevation measurements or obtained from multiple pressure sensors distributed over the wetted surface of the WEC. In addition to the challenge of obtaining reliable wave elevation measurements in real sea-scenarios [11], a major drawback of these estimators is that they are not able to consider measurement or model uncertainties. The quality of the estimation therefore depends on the quality of the measurement signals and the accuracy of the used models [10]. As a result, model-based closed-loop estimators are usually preferred.

1.2.1 Estimation based on 1DoF models

Most strategies proposed for point absorbers rely on models that represent the dynamics of the WEC by a single degree of freedom (1DoF). The most commonly used approach is the implementation of Kalman filters based on linearized dynamics, see, e.g., [12–14]. Measurements of position and velocity are usually taken. The dynamics of the excitation force is represented using either a random walk model or a harmonic oscillator model, often incorporating multiple oscillators of different frequencies. Although the use of multiple oscillators increases the complexity of the estimation problem, it is often preferred as it provides a more accurate representation of the behavior of ocean waves, see [15]. Nonetheless, the accuracy of the estimation still depends on the number of oscillators and the selected frequencies. To address this issue, estimators have been proposed in the literature that treat the excitation force as an unknown input without considering any dynamics [16–18]. A detailed comparison between these estimators and Kalman filter approaches is provided in [15]. The results show that there is no significant difference in either computational effort or accuracy. Another estimator that considers the excitation force as an unknown input is the receding horizon estimator, presented in [14], where the excitation force is estimated by solving a quadratic programming problem. In an experimental setup, Nguyen and Tona [14] show that the receding horizon approach provides slightly better results compared to the Kalman filter, which uses a random walk model for the excitation force. However, this improvement comes at the expense of increased computational effort. A commonly used approach in the numerical modelling of WECs is to consider nonlinear viscous drag terms [19]. For this reason, the Kalman filter-based strategies were adapted in [20] to incorporate these nonlinearities, resulting in the design of extended Kalman filters. According to Davis and Fabien [20], good estimates are obtained using wave tank data. The extended Kalman filter based on a harmonic oscillator model for the excitation force demonstrated enhanced accuracy compared to the filter based on a random walk model [20]. It should be noted, that the tank tests were conducted under uncontrolled conditions of the floating body and without a comparison to a linear Kalman filter. A different extended Kalman filter approach is proposed in [21]. In addition to position measurements, this approach incorporates pressure measurements at specific points on the buoy, which should increase the estimation accuracy for the excitation force. However, as shown in [15], this method does not provide any improvements over other strategies, at least under linear wave conditions. In various studies, the estimation strategies presented have only been validated using 1DoF simulation models. While in [14], a 1DoF estimation model appears to be applicable due to the restricted kinematics of the WEC, the suitability of 1DoF estimators for real WECs with more complex dynamics is questionable.

1.2.2 Estimation based on multi-DoF models

Despite the importance of estimating the excitation force, the existing literature on estimation models considering multiple degrees of freedom (multi-DoF) is still limited. The use of Kalman filters based on 3DoF WEC models is demonstrated in [22–24]. In [22, 23], the Kalman filters rely on linear dynamics of the WEC, while in [24], nonlinear

couplings between the degrees of freedom are considered. In addition to the Kalman filter, an artificial neural network approach for estimating the excitation force is proposed in [23]. A comparison shows that the accuracy for both the artificial neural network and Kalman filter are similar [23]. It should be noted, that the estimation strategies [22–24] have all been validated using 3DoF simulation models, which differ only slightly from the estimation models used. Probably the most comprehensive approach in the literature currently is the use of a cubature Kalman filter based on a linearized 6DoF WEC model in [25]. Similar to the unscented Kalman filter, the cubature Kalman filter estimates the state of a dynamic system based on a set of sample points that follow the cubature rule derived by Arasaratnam and Haykin [26]. The presented approach in [25] is able to estimate a 6-dimensional excitation force vector and shows promising results in terms of multidirectional wave simulations. However, it comes with the burden of using a dynamic system of order 72.

1.3 Goals of this Thesis

To the best of the author's knowledge, there is currently no estimation strategy that accounts for non-linearities resulting from the variable submergence of the buoy, caused by the changing wave elevation and buoy position. As shown in [27, 28], such non-linearities can have a significant impact on hydrodynamic forces and thus on the model accuracy for semi-submerged WECs. The instantaneous wave elevation is also considered in the C4 control model in order to account for certain non-linearities. Hence, the objective is to develop an estimation strategy that is capable of estimating not only the excitation force but also the wave elevation. Furthermore, the reliability of the estimation is important for the optimal operation of the WEC. Thus, potential sensors should be included in the estimation process to achieve fault tolerance in case of sensor failures. An investigation of the estimation accuracy and robustness against sensor failures should be conducted.

1.4 Content and Structure

The structure of this thesis is as follows. Chapter 2 gives a brief overview of the relevant hydrodynamic theories together with the simulation setup used for the validation. In addition, the sensors used for the estimation are briefly presented. Chapter 3 covers the mathematical modeling. This involves deriving a model that represents the relevant dynamics of the WEC, which is subsequently simplified and verified with numerical simulations. A harmonic oscillator model is introduced to describe the wave process, providing approximations for the wave elevation and excitation force. Furthermore, the relevant sensor models are derived. Chapter 4 covers the observer design based on the derived models. The estimation performance of the observer is then evaluated using a comprehensive simulation model. The results include an evaluation of the estimation performance across various sea states, as well as a comparison with the estimation strategy currently used by the company CorPower Ocean. In addition, the robustness of the observer in case of different sensor failures is investigated and discussed. In a further analysis, the influence of the degrees of freedom considered in the estimation model on

the estimation errors are analyzed. Chapter 5 provides a conclusion and outlook of this thesis with possible ideas for future work.

2 Theory and Simulation Setup

In this chapter, the fundamental theory and simulation setup are outlined. Firstly, the principles of linear wave theory are introduced. Linear wave theory serves as the basis for the simulation setup and is essential for modeling the wave process and the hydrodynamic pressure, both of which are relevant for the estimation task. Next, a brief explanation of the relevant hydrodynamic and hydrostatic forces is provided, which are relevant for the derivation of the WEC model. Additionally, key aspects of the simulation setup and a brief overview of the sensors used for the estimation are presented.

2.1 Linear Wave Theory

Linear wave theory is used to model the wave process in the ocean, which covers the vast majority of waves in power production of WECs [29]. Additional research on the validity and constraints of analytical wave theories can be found in [30] and [31]. Linear wave theory relies on a mass balance equation and a momentum balance equation, both of which can be expressed in terms of a velocity potential function Φ [32]. Assuming the fluid to be incompressible and irrotational, one obtains the Laplace equation from the mass balance equation

$$\Delta\Phi = 0. \quad (2.1)$$

Neglecting quadratic velocity terms in the momentum balance equation yields the linearized Bernoulli equation for unsteady flow [32]

$$\frac{\partial}{\partial t}\Phi + \frac{p}{\rho} + gz = 0, \quad (2.2)$$

where p is the pressure, ρ is the water density, g is the gravitational acceleration, and z is the vertical distance to the water surface. The positive z -axis is opposite to the direction of gravity, the x - and y -axes are parallel to the earth's surface. Solving the Laplace equation considering linearized kinematic and dynamic boundary conditions for the seabed and the water surface (see [32]), an analytical solution for the boundary condition of the water surface can be found. One solution is characterized by a monochromatic wave with the amplitude A and angular frequency ω , propagating in the positive x -direction [32]

$$\eta(x, t) = A \sin(\omega t - kx), \quad (2.3)$$

where η is the free surface elevation or wave elevation of the harmonic wave and k is the spatial frequency, the so-called wave number. The corresponding solution for the velocity potential function provides information on the wave-induced motion beneath the water surface and is expressed as [32]

$$\Phi(x, z, t) = \frac{A\omega}{k} \frac{\cosh(k(d+z))}{\sinh(kd)} \cos(\omega t - kx), \quad (2.4)$$

where d is the water depth. The relation between the wave number k and the angular frequency ω is determined by the dispersion relationship [32]

$$\omega^2 = gk \tanh(kd). \quad (2.5)$$

Each wave number therefore has its own angular frequency, i.e. the speed at which a wave propagates depends on the wavelength.

Besides the simplicity of linear wave theory in describing the wave-induced behavior, a further important advantage is that linear superposition holds. This allows an irregular wave, as it occurs in the ocean, to be expressed as a sum of regular wave components [33]. Thus, the wave elevation of an irregular wave, denoted as ζ , at the chosen location $x = 0$ can be expressed using (2.3) as

$$\zeta(t) = \sum_{i=1}^N \eta_i \quad \text{with} \quad \eta_i = A_i \sin(\omega_i t + \alpha_i). \quad (2.6)$$

The phase components α_i are typically uniformly distributed between 0 and 2π , so that the phase spectrum may be ignored [34]. The amplitude components A_i can be determined using an energy density spectrum, which is a function of the angular frequency components ω_i , characterizing the sea state. The spectrum is usually defined with several parameters, where the most important ones are the significant wave height and the peak wave period or energy period [6].

2.2 Hydrodynamic and Hydrostatic Forces

As discussed in the study [35], various techniques exist for calculating the hydrodynamic forces experienced by a body undergoing oscillations in water. In the context of wave energy converters, a common approach is to use linear wave theory and linear potential flow theory to represent the overall hydrodynamic force \mathbf{F}_{hyd} . This force is composed of four distinct forces and expressed as

$$\mathbf{F}_{hyd} = \mathbf{F}_e + \mathbf{F}_r + \mathbf{F}_b + \mathbf{F}_d, \quad (2.7)$$

where \mathbf{F}_e denotes the excitation force, \mathbf{F}_r the radiation force, \mathbf{F}_b the buoyancy force due to the hydrostatic pressure, and \mathbf{F}_d the nonlinear drag force commonly used in WEC modeling.

2.2.1 Excitation Force

The excitation force describes the force induced by both the undisturbed incident wave and the wave scattered through the body. These two components are also known as the dynamic Froude-Krylov force and diffraction force [36]. Utilizing linear wave theory, the excitation force is calculated by the convolution product between the excitation impulse response function $\mathbf{f}_{e,t}$ and the wave elevation ζ [36], resulting in

$$\mathbf{F}_e = \int_{-\infty}^{\infty} \mathbf{f}_{e,t}(t - \tau) \zeta(\tau) d\tau. \quad (2.8)$$

It is worth mentioning that the impulse response function is not necessarily causal [36], which would require future wave elevation values to calculate the instantaneous excitation force. However, the magnitude and phase responses of the excitation force at a given frequency of a regular wave can be obtained using a boundary element method (BEM), e.g. WAMIT [37]. Consequently, the j^{th} component of the excitation force vector resulting from an irregular wave can also be expressed using the definition from (2.6), without using future wave elevation values. With $F_{e,j}$ representing the j^{th} component of the excitation force vector, this leads to

$$F_{e,j} = \sum_{i=1}^N A_{e,j}(\omega_i) A_i \sin(\omega_i t + \alpha_i + \alpha_{e,j}(\omega_i)), \quad (2.9)$$

where $A_{e,j}(\omega_i)$ and $\alpha_{e,j}(\omega_i)$ denote the corresponding magnitude and phase response of the excitation force as a function of the wave frequency. Note that (2.9) is unaffected by the WEC's motion.

2.2.2 Radiation Force

The radiation force is expressed according to Cummins' equation [38] as

$$\mathbf{F}_r = -\mathbf{M}_\infty \ddot{\boldsymbol{\xi}} - \int_{-\infty}^{\infty} \mathbf{K}_r(t - \tau) \dot{\boldsymbol{\xi}}(\tau) d\tau, \quad (2.10)$$

with $\boldsymbol{\xi}$ being a six-dimensional vector containing the position and orientation of the WEC with respect to a reference frame. This force originates from the body's oscillation in water and is decomposed into two components: The first component is proportional to the body's acceleration $\ddot{\boldsymbol{\xi}}$, computed using the infinitely added mass matrix \mathbf{M}_∞ , which characterizes the mass of water entrained by the body's movement. The second component describes the damping force proportional to the velocity of the body $\dot{\boldsymbol{\xi}}$, calculated by the convolution product with the radiation impulse response matrix \mathbf{K}_r . For efficient computation, the convolution term is commonly approximated with a state space model [39, 40]

$$\dot{\mathbf{x}}_r = \mathbf{A}_r \mathbf{x}_r + \mathbf{B}_r \dot{\boldsymbol{\xi}} \quad (2.11)$$

$$\mathbf{F}_{r,l} = \mathbf{c}_r^T \mathbf{x}_r. \quad (2.12)$$

The output $\mathbf{F}_{r,l}$ is from now on referred to as the radiation force with

$$\mathbf{F}_r \approx -\mathbf{M}_\infty \ddot{\boldsymbol{\xi}} + \mathbf{F}_{r,l}. \quad (2.13)$$

The coefficients for the state space model and the added mass matrix used in the WEC model in Section 3.1, are obtained from pre-calculated data by WAMIT.

2.2.3 Nonlinear Extension and Buoyancy Force

As demonstrated in [27, 28], considering non-linearities in both buoyancy and dynamic Froude-Krylov force can significantly improve the model accuracy, especially given their

dominance over the radiation and diffraction force for heaving point absorbers. In this thesis, nonlinear extensions for the buoyancy force and the excitation force are used. These extensions account for the instantaneous submergence of the WEC $V_{sub}(t)$. The buoyancy force follows to [41]

$$\mathbf{F}_b = \rho g V_{sub}(t) \mathbf{e}_z \quad \text{with} \quad \mathbf{e}_z^T = [0 \ 0 \ 1], \quad (2.14)$$

and the modified excitation force $\check{\mathbf{F}}_e$ is expressed as [41]

$$\check{\mathbf{F}}_e = \mathbf{f}_e(\zeta, V_{sub}(t), \mathbf{F}_e). \quad (2.15)$$

Based on the small-body approximation [36], the formulation of the excitation force \mathbf{F}_e in (2.15) is corrected based on the instantaneous submerged volume. As a result, the modified force $\check{\mathbf{F}}_e$ is not only dependent on the wave elevation (cf. (2.9)), but also on the position of the WEC. This also allows the effects of mean drift forces to be captured [6]. For reasons of confidentiality, the modified force is not described in more detail.

2.2.4 Drag Force

Nonlinear viscous drag forces are modeled according to the Morison equation [42, 43]. Let \circ and $\circ^{\frac{1}{2}}$ denote the Hadamard product (element-wise product) and Hadamard square root (element-wise square root) [44]. Under the assumption of neglecting the fluid particle velocity, the drag force vector can be approximated as

$$\mathbf{F}_d = -\frac{1}{2} \rho \mathbf{A}_d \mathbf{C}_d \left(\dot{\boldsymbol{\xi}} \circ \dot{\boldsymbol{\xi}} \right)^{\circ^{\frac{1}{2}}} \circ \dot{\boldsymbol{\xi}}, \quad (2.16)$$

where matrix \mathbf{C}_d contains the drag coefficients, and the matrix \mathbf{A}_d the submerged surfaces of the body projected on the plane perpendicular to the direction of motion.

2.3 Wave-to-Wire Model

The term wave-to-wire (W2W) refers to numerical tools capable of modeling the entire chain of energy conversion from the hydrodynamic wave/device interaction to feeding into the electrical grid [6]. CorPowe Oceans's W2W model is a 6-degree-of-freedom model implemented in MATLAB/SIMULINK and is the most comprehensive simulation model of the WEC available within the company. Therefore, it will be used to validate the performance of the estimation. The exogenous inputs to the W2W model include the wave elevation based on linear wave theory and the pre-calculated excitation force as described in Section 2.2.1. Thus, the estimation is evaluated by comparing these inputs with the corresponding estimates of these quantities. The simulation model can be executed using regular waves or irregular waves. As CorPower's testing site is situated in Agucadoura, Portugal, the predominant energy density spectra at this location are used for characterizing the sea states and simulating irregular waves. The JONSWAP (Joint North Sea Wave Project) spectrum [45] serves as a mathematical representation of the energy density spectrum, parameterized by the significant wave height H_s and the

energy period T_e . Figure 2.1 shows the probability of occurrence of the resulting sea states for Agucadoura. Sea states covered by the dashed border indicate the region in which the WEC is in tuned mode. Thus, these sea states are considered for validation of the estimation.

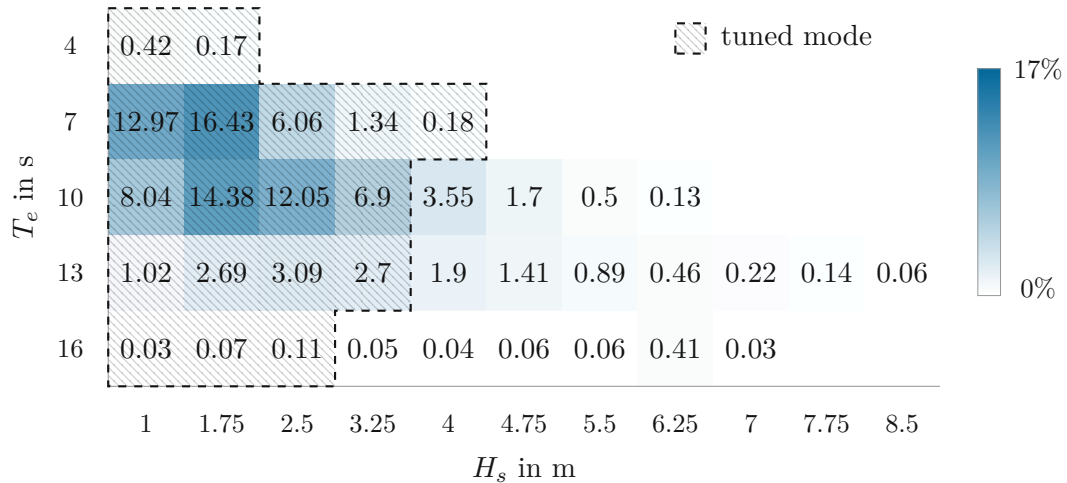


Figure 2.1: Probability of sea states for Agucadoura (%) [46]

2.4 Sensors

The following sensors are available for the estimation task: two inertial measurement units (IMUs), one encoder and one pressure sensor. Figure 2.2 gives an overview of the location of these sensors. One IMU is attached to the buoy, capturing its oscillating behaviour. The second IMU is fixed to the stationary part inside the buoy, capturing only the lateral movements of the WEC. The IMUs provide measurements of acceleration and angular rates as well as estimates of the sensor attitude. The absolute encoder is mounted on a circular gear (pinion) of the gearbox that engages with the rack and provides feedback on the absolute position of the rack. The pressure sensor is a piezoresistive pressure transmitter with a total measurement range of 0-3bar and a maximum error of $\pm 0.01\%$ of the total measurement range. As indicated in Figure 2.2, the sensor is installed below the ocean rods on the so-called ocean plate, where it captures the hydrodynamic pressure induced by the ocean waves. The sensor characteristics based on the data sheets and measurements are added to the simulated sensor signals for a more realistic evaluation of the estimators. The characteristics of the sensors are discussed in more detail in Section 3.3.

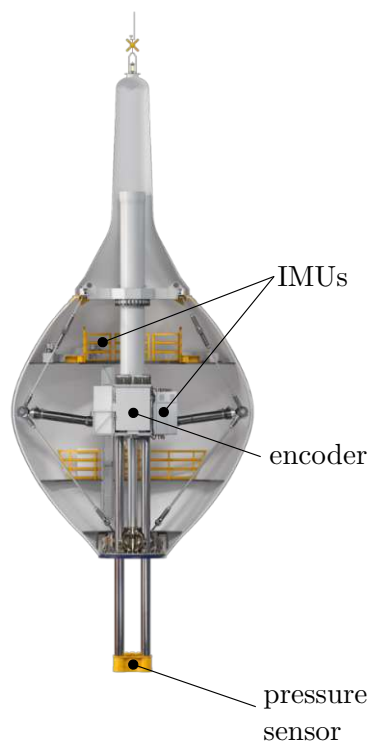


Figure 2.2: Location of the sensors [7]

3 Mathematical Modeling

This chapter deals with the mathematical models required for the estimation task. A non-linear dynamic model of the WEC is derived on the basis of the relevant kinematics. This model is then simplified and verified by numerical simulations. In addition, a harmonic oscillator model is introduced, which is necessary for the description of the wave process and from which the wave elevation and the excitation force are obtained. Finally, sensor models for the sensors are derived.

3.1 WEC Model

In preparation for deriving the kinematics and dynamics of the wave energy converter, an overview of the mechanical and hydromechanical properties, along with relevant assumptions and notations is presented first.

3.1.1 Assumptions and Notations

Assuming that the flexibility of the mooring rod can be neglected, the wave energy converter can be modeled using two rigid bodies - one oscillating and one stationary, which is only deflected laterally due to the incoming waves, see Figure 3.1. It is worth mentioning that the effects due to the flexibility of the mooring rod are included in CorPower Ocean's W2W model. To demonstrate the negligible impact of the mooring rod, as shown in Section 3.1.5, it is treated as a separate rigid body. To do so, the stationary body is split into the *slide* and the *rod*. The oscillating body, referred to as the *buoy*, is characterized by a mass m_B . The slide, which comprises all stationary components inside the hull, including the ocean rods, has a mass of m_S . The moment of inertia of the buoy and slide are neglected due to two reasons. Firstly, the WEC's movement around the symmetry axis is irrelevant when describing its motion. This degree of freedom will also be disregarded in the following description of the kinematics in Section 3.1.2. Secondly, due to the length of the rod, the effect of the inertia is relatively small compared to the impact of the masses. This is confirmed when applying Steiner's theorem about the axes of the universal joint [47]. Only for the rod, the inertia matrix \mathbf{I}_R is taken into account in addition to its mass m_R . Furthermore, the inertia of the transmission to the rack within the gearbox is considered and denoted as I_{trans} . With d_{mwl} , the distance from the space-fixed inertial frame $[0_I, x_I, y_I, z_I]$ to the mean water level is defined. The mean water level refers to the average height of water in the absence of waves.

To fully describe the dynamics of the WEC in the ocean, additional hydromechanical properties are relevant. It is essential to account for added mass effects resulting from the radiation force outlined in Section 2.2.2. Due to the low angular velocities of the

WEC, only the radiation force components that arise due to its linear accelerations and velocities are taken into account. Hence, the infinitely added mass matrix \mathbf{M}_∞ as a result of the linear accelerations is assigned to the buoy. Due to the small volume of the slide and rod compared to the buoy, they are assumed to have a negligible radiation force and, consequently, negligible added mass effects. The center of buoyancy is defined as the center of gravity of the displaced fluid [48] and is used as the point of attack for the buoyancy forces. The center of buoyancy, denoted as cb , for the buoy (B), the slide (S), and the rod (R) is illustrated in Figure 3.1. The hydrodynamic forces are also assumed to act at the center of buoyancy, which is a common assumption in the small body approximation [36]. While the center of buoyancy of the rod is constant with respect to its body-fixed coordinate frame, it will change for the slide and the buoy due to the variable submergence. However, it is assumed that the relative change in the center of buoyancy of the slide and buoy in relation to the total length of the rod (30m) is comparable small. Hence, they are considered to be constant with respect to their body-fixed coordinate frame. As often used in the context of maritime and naval engineering and as indicated in Figure 3.1, the linear motion of the WEC in x -, y - and z -direction are referred to as the surge, sway and heave direction [6].

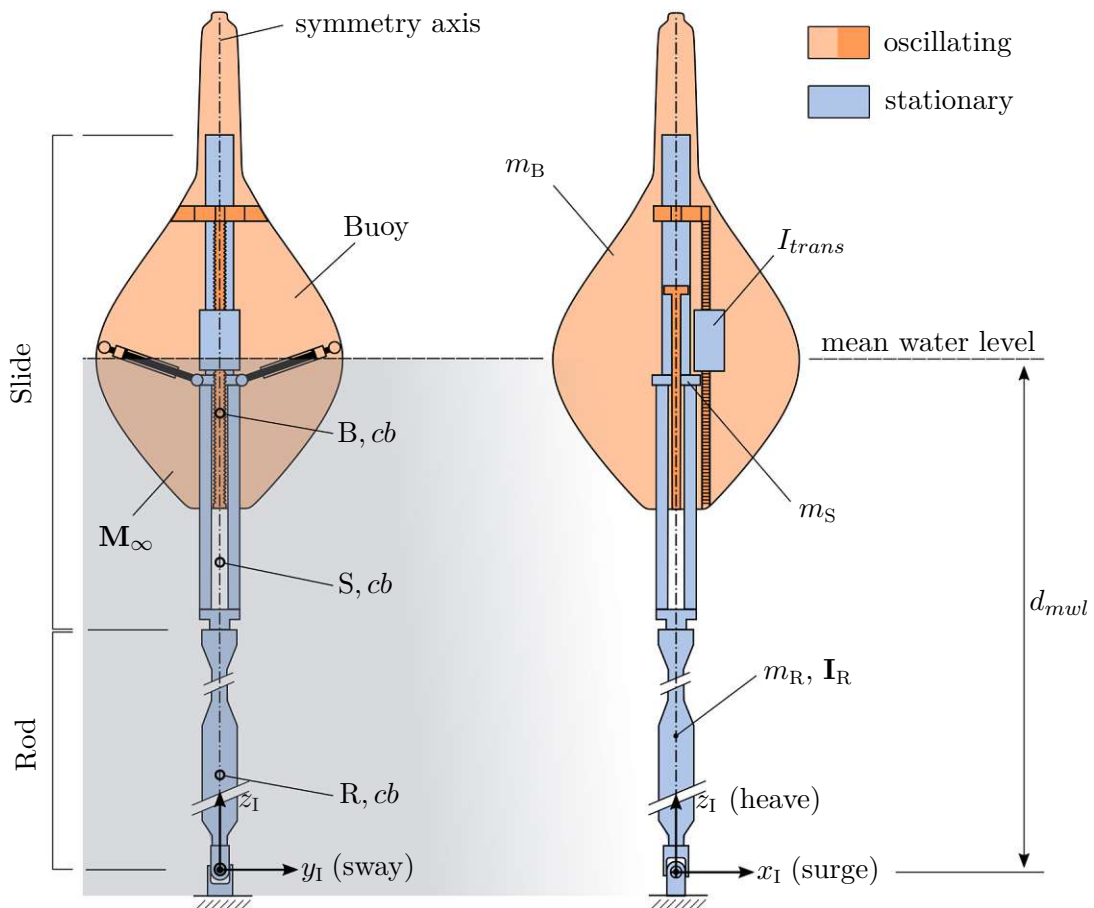


Figure 3.1: Schematic representation of the WEC

3.1.2 Kinematics

Degrees of Freedom

As mentioned in the previous section, the flexibility of the rod and motion of the WEC around the symmetry axis are disregarded. As a result, the remaining motion of the WEC can be characterized with three degrees of freedom and are expressed using the vector of generalized coordinates

$$\mathbf{q} = \begin{bmatrix} s_{rack} \\ \varphi \\ \theta \end{bmatrix}. \quad (3.1)$$

The first degree of freedom describes the buoy's movement relative to the slide, representing the rack's position, and is denoted as s_{rack} . The other two degrees of freedom are associated with the universal joint, labeled as φ and θ . These angles correspond to the WEC's roll and pitch angles, respectively. In Figure 3.2, the kinematic model of the WEC illustrates these degrees of freedom.

Coordinate Frames and Transformations

To describe the kinematics of the WEC, three local coordinate frames are used, as shown in Figure 3.2 b). The coordinate frame attached to the buoy is represented by $[0_B, x_B, y_B, z_B]$; the frame used to describe the slide is denoted by $[0_S, x_S, y_S, z_S]$. Since the slide and rod could be treated as a single rigid body, the coordinate frame of the slide can be used to describe the kinematics of the rod. However, in order to determine external torques on the rod, e.g. due to drag, a third local coordinate frame for the rod ($[0_R, x_R, y_R, z_R]$) is introduced. The kinematic relations between the coordinate frames are derived using the Denavit-Hartenberg (DH) convention. The DH parameters as defined in [49] are listed in Table 3.1. Their corresponding coordinate frames are shown in Figure 3.2 a).

Link	a_i	α_i	d_i	ϑ_i
1	0	$\frac{\pi}{2}$	0	θ
2	0	$\frac{\pi}{2}$	d_S	$\frac{\pi}{2} - \varphi$
3	0	0	s_{rack}	$-\frac{\pi}{2}$

Table 3.1: Denavit-Hartenberg parameters

Applying the DH convention, the homogeneous transformation matrices $\mathbf{H}_0^1(\varphi, \theta)$, $\mathbf{H}_0^2(\varphi, \theta)$ and $\mathbf{H}_0^3(\mathbf{q})$ are derived to establish a relation between the local coordinate frames $[0_1, x_1, y_1, z_1]$, $[0_2, x_2, y_2, z_2]$, and $[0_3, x_3, y_3, z_3]$ with the space-fixed coordinate frame $[0_0, x_0, y_0, z_0]$. Since the coordinate frames shown in Figure 3.2 b) are to be used for the WEC model, the homogeneous transformation matrices $\mathbf{H}_1^B(\mathbf{q})$, $\mathbf{H}_1^S(\varphi, \theta)$ and $\mathbf{H}_1^R(\varphi, \theta)$

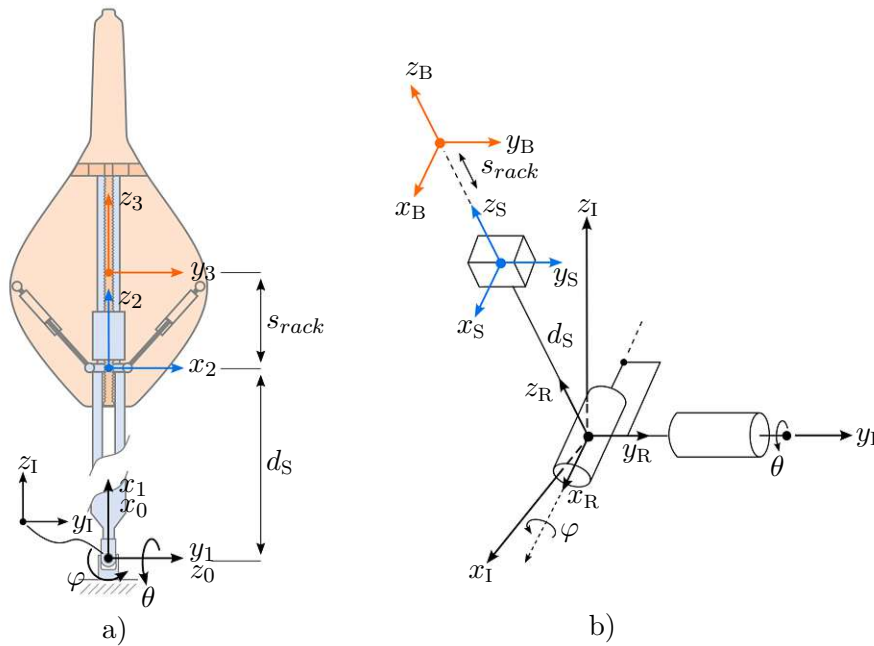


Figure 3.2: Kinematic model of WEC: a) coordinate frames according to DH convention
b) used coordinate frames for model

can be computed as

$$\mathbf{H}_1^B(\mathbf{q}) = \mathbf{H}_0^3(\mathbf{q})\mathbf{H}_1^0, \quad (3.2a)$$

$$\mathbf{H}_1^S(\varphi, \theta) = \mathbf{H}_2^S\mathbf{H}_0^2(\varphi, \theta)\mathbf{H}_1^0, \quad (3.2b)$$

$$\mathbf{H}_1^R(\varphi, \theta) = \mathbf{H}_1^R\mathbf{H}_0^1(\varphi, \theta)\mathbf{H}_1^0, \quad (3.2c)$$

with \mathbf{H}_1^0 , \mathbf{H}_2^S and \mathbf{H}_1^R being constant homogeneous transformation matrices.

Positions and Linear Velocities

To obtain the position vectors and linear velocities of the center of gravity's (*cg*) in the space-fixed inertial frame, first the homogeneous representation of the constant position vector $\mathbf{p}_i^{i, cg} \in \mathbb{R}^{3 \times 1}$ in the body-fixed coordinate frame i is defined as

$$\tilde{\mathbf{p}}_i^{i, cg} = \begin{bmatrix} \mathbf{p}_i^{i, cg} \\ 1 \end{bmatrix}, \quad i \in \mathcal{B}, \quad (3.3)$$

with the set of bodies $\mathcal{B} = \{B, S, R\}$. Using the transformation matrices from (3.2), these vectors are transformed into the space-fixed inertial frame with

$$\tilde{\mathbf{p}}_1^{i, cg} = \begin{bmatrix} \mathbf{p}_1^{i, cg} \\ 1 \end{bmatrix} = \mathbf{H}_1^i \tilde{\mathbf{p}}_i^{i, cg}, \quad i \in \mathcal{B}, \quad (3.4)$$

where $\mathbf{p}_I^{i,cg}$ is the position vector of the center of gravity of body i , expressed in the inertial frame. Taking the time derivative of this vectors gives the velocity in the inertial frame as

$$\mathbf{v}_I^{i,cg} = \frac{d}{dt} \mathbf{p}_I^{i,cg}, \quad i \in \mathcal{B} \quad (3.5)$$

Analogously, equations (3.3) to (3.5) are used to derive the position vectors and linear velocities of the center of buoyancy's expressed in the inertial frame with $\mathbf{p}_I^{i,cb}$ and $\mathbf{v}_I^{i,cb}$ respectively.

Rotations and Angular Velocities

The rotation matrix $\mathbf{R}_I^i \in SO(3)$ of the coordinate frame i with respect to the inertial frame can be extracted from the homogeneous transformation matrices defined in (3.2), which can be written as

$$\mathbf{H}_I^i = \begin{bmatrix} \mathbf{R}_I^i & \mathbf{d}_I^i \\ \mathbf{0}^T & 1 \end{bmatrix}, \quad i \in \mathcal{B}, \quad (3.6)$$

with the vector $\mathbf{d}_I^i \in \mathbb{R}^{3 \times 1}$ describing the origin of frame i expressed in the inertial frame. The angular velocities $\boldsymbol{\omega}_I^i$ of the coordinate frame i described in the inertial frame are obtained using the skew-symmetric matrix $\mathbf{S}(\boldsymbol{\omega})$ [50]. The elements of

$$\mathbf{S}(\boldsymbol{\omega}_I^i) = \dot{\mathbf{R}}_I^i (\mathbf{R}_I^i)^T = \begin{bmatrix} 0 & -\omega_{I,z}^i & \omega_{I,y}^i \\ \omega_{I,z}^i & 0 & -\omega_{I,x}^i \\ -\omega_{I,y}^i & \omega_{I,x}^i & 0 \end{bmatrix}, \quad i \in \mathcal{B}, \quad (3.7)$$

can be used to form the angular velocity vector

$$\boldsymbol{\omega}_I^i = \begin{bmatrix} \omega_{I,x}^i \\ \omega_{I,y}^i \\ \omega_{I,z}^i \end{bmatrix}, \quad i \in \mathcal{B}. \quad (3.8)$$

Geometric Jacobian

To compute the corresponding generalized forces from the external forces and moments, the geometric Jacobian matrices are used [50]. The geometric Jacobian of linear velocities of the center of gravity and center of buoyancy follow as

$$(\mathbf{J}_v)_I^{i,cg} = \frac{\partial \mathbf{p}_I^{i,cg}}{\partial \mathbf{q}}, \quad i \in \mathcal{B}. \quad (3.9a)$$

$$(\mathbf{J}_v)_I^{i,cb} = \frac{\partial \mathbf{p}_I^{i,cb}}{\partial \mathbf{q}}, \quad i \in \mathcal{B}. \quad (3.9b)$$

Similarly, the geometric Jacobian of angular velocities can be calculated by

$$(\mathbf{J}_\omega)_I^i = \frac{\partial \boldsymbol{\omega}_I^i}{\partial \dot{\mathbf{q}}}, \quad i \in \mathcal{B}. \quad (3.10)$$

Note that the following applies

$$(\mathbf{J}_\omega)_I^B = (\mathbf{J}_\omega)_I^S = (\mathbf{J}_\omega)_I^R. \quad (3.11)$$

3.1.3 Dynamics

Utilizing the results from the previous section, the equations of motion for the WEC can be derived using the Euler-Lagrange formalism [49]. When all forces are regarded as external generalized forces, the Euler-Lagrange equations can be formulated as

$$\frac{d}{dt} \frac{\partial}{\partial \dot{r}} T - \frac{\partial}{\partial r} T = f_r, \quad (3.12a)$$

$$\frac{d}{dt} \frac{\partial}{\partial \dot{\varphi}} T - \frac{\partial}{\partial \varphi} T = f_\varphi, \quad (3.12b)$$

$$\frac{d}{dt} \frac{\partial}{\partial \dot{\theta}} T - \frac{\partial}{\partial \theta} T = f_\theta, \quad (3.12c)$$

with the total kinetic energy T and the external generalized forces f_r , f_φ , and f_θ . Taking into account the assumptions made in Section 3.1.1, the total kinetic energy of the system can be expressed as

$$\begin{aligned} T = & \underbrace{\frac{1}{2} (\mathbf{v}_I^{B,cg})^T \mathbf{M}_{B,\infty} \mathbf{v}_I^{B,cg}}_{T_B} + \underbrace{\frac{1}{2} m_S (\mathbf{v}_I^{S,cg})^T \mathbf{v}_I^{S,cg}}_{T_S} \\ & + \underbrace{\frac{1}{2} m_R (\mathbf{v}_I^{R,cg})^T \mathbf{v}_I^{R,cg} + \frac{1}{2} (\boldsymbol{\omega}_I^R)^T \mathbf{R}_I^R \mathbf{I}_R (\mathbf{R}_I^R)^T \boldsymbol{\omega}_I^R}_{T_R} + \underbrace{\frac{1}{2} I_{trans} \omega_{gen}^2}_{T_{trans}}. \end{aligned} \quad (3.13)$$

In (3.13), T_B denotes the kinetic energy of the buoy with the matrix

$$\mathbf{M}_{B,\infty} = m_B + \mathbf{M}_\infty = \begin{bmatrix} m_B + m_{\infty,xy} & 0 & 0 \\ 0 & m_B + m_{\infty,xy} & 0 \\ 0 & 0 & m_B + m_{\infty,z} \end{bmatrix}, \quad (3.14)$$

comprising the mechanical mass and the added mass in surge, sway, and heave direction. Due to the symmetry of the buoy, the added mass for surge and sway ($m_{\infty,xy}$) are equal. T_S and T_R represent the kinetic energy of the slide and the rod, respectively. The kinetic energy of the transmission is labeled as T_{trans} , wherein ω_{gen} describes the angular velocity of the generators. Its relation with the rack position is given as

$$\omega_{gen} = \frac{u_{gbx}}{r_{pin}} \dot{s}_{rack}, \quad (3.15)$$

where u_{gbx} refers to the transmission ratio of the gearbox, and r_{pin} describes the radius of the pinion that engages the rack. Substituting equation (3.13) into (3.12) leads to the equations of motion, which can be represented in the compact way

$$\mathbf{D}(\mathbf{q})\ddot{\mathbf{q}} + \mathbf{C}(\mathbf{q}, \dot{\mathbf{q}})\dot{\mathbf{q}} = \mathbf{f}_q \quad \text{with} \quad \mathbf{f}_q = \begin{bmatrix} f_r \\ f_\varphi \\ f_\theta \end{bmatrix}. \quad (3.16)$$

In (3.16), $\mathbf{D}(\mathbf{q})$ represents the mass matrix of the system, while the matrix $\mathbf{C}(\mathbf{q}, \dot{\mathbf{q}})$ contains the centrifugal and Coriolis terms. To calculate the vector of generalized forces \mathbf{f}_q , the external forces need to be derived.

3.1.4 External Forces

Gravitational and Buoyancy Force

First, the forces due to gravity in the inertial frame are calculated. The force, which arises from the weight of the bodies, is given as

$$\mathbf{F}_{g,i} = m_i \begin{bmatrix} 0 \\ 0 \\ -g \end{bmatrix}, \quad i \in \mathcal{B}. \quad (3.17)$$

The buoyancy force, as defined in (2.14), follows to

$$\mathbf{F}_{b,i} = V_{sub,i} \begin{bmatrix} 0 \\ 0 \\ \rho g \end{bmatrix}, \quad i \in \mathcal{B}. \quad (3.18)$$

Since the rod is fully submerged, its submerged volume $V_{sub,R}$ remains constant and is equal to the volume of the rod. The submerged volume of the slide denoted as $V_{sub,S}$, is calculated in the equilibrium position of the WEC and assumed to be constant. The reason for this is that the volume of the slide is relatively small compared to the volume of the buoy and thus has little influence.

Next, an approximation of the instantaneous submerged volume of the buoy is derived. As the primary buoy motion occurs in the heave direction, a suitable approximation for the submerged volume can be obtained by considering only the z -position of the buoy z_1^B and the wave elevation (ζ). Assuming a constant wave elevation above the buoy, the volume is approximated by a polynomial function of order N in the form

$$V_{sub,B} = \sum_{i=0}^N p_i \left(\zeta - \underbrace{(\mathbf{e}_z^T \mathbf{d}_I^B}_{z_1^B} - d_{mwl}) \right)^i. \quad (3.19)$$

Drag Force

Drag forces are considered as described in Section 2.2.4. Due to the relatively small deflections of the buoy in roll and pitch direction, the drag forces of the buoy are approximated using the linear velocities. Hence, according to (2.16), the drag force vector in Cartesian coordinates of the buoy calculates to

$$\mathbf{F}_{d,B} = -\frac{1}{2} \rho \mathbf{A}_{d,B} \mathbf{C}_{d,B} \left(\mathbf{v}_I^{B,cb} \circ \mathbf{v}_I^{B,cb} \right)^{\circ \frac{1}{2}} \circ \mathbf{v}_I^{B,cb}, \quad (3.20)$$

with matrices of the projected surface and drag coefficient defined as

$$\mathbf{A}_{d,B} = \begin{bmatrix} A_{B,xy} & 0 & 0 \\ 0 & A_{B,xy} & 0 \\ 0 & 0 & A_{B,z} \end{bmatrix} \quad \text{and} \quad \mathbf{C}_{d,B} = \begin{bmatrix} C_{B,xy} & 0 & 0 \\ 0 & C_{B,xy} & 0 \\ 0 & 0 & C_{B,z} \end{bmatrix}. \quad (3.21)$$

The elements of the matrix $\mathbf{A}_{d,B}$ are calculated in the equilibrium position of the WEC and are assumed to be constant. The drag of the slide in the heave direction is negligible. The resulting drag force of the slide is calculated similar to (3.20) as

$$\mathbf{F}_{d,S} = -\frac{1}{2}\rho A_{d,S} \mathbf{C}_{d,S} \left(\mathbf{v}_1^{S,cb} \circ \mathbf{v}_1^{S,cb} \right)^{\circ \frac{1}{2}} \circ \mathbf{v}_1^{S,cb}, \quad (3.22)$$

with the constant projected surface $A_{d,S}$ for surge and sway direction, and the matrix of drag coefficients

$$\mathbf{C}_{d,S} = \begin{bmatrix} C_{S,xy} & 0 & 0 \\ 0 & C_{S,xy} & 0 \\ 0 & 0 & 0 \end{bmatrix}. \quad (3.23)$$

For the rod, drag forces are considered by assigning drag torques around the rod's x - and y -axes. As shown in [51], viscous damping effects due to angular motion can be considered by integrating the forces over the entire surface. Assuming the constant cross-section area A for the rod, (2.16) is used to define the force acting on the surface area dA at length l with

$$d\mathbf{F}_{d,R}(l) = -\frac{1}{2}\rho C_{d,R} \left(\mathbf{v}_R^R(l) \circ \mathbf{v}_R^R(l) \right)^{\circ \frac{1}{2}} \circ \mathbf{v}_R^R(l) dA. \quad (3.24)$$

The linear velocity of the rod as a function of the length l is defined by the cross product (\times) of the angular velocity and the distance vector \mathbf{l}_R as

$$\mathbf{v}_R^R(l) = \left(\left(\mathbf{R}_I^R \right)^T \boldsymbol{\omega}_I^R \right) \times \mathbf{l}_R \quad \text{with} \quad \mathbf{l}_R = \begin{bmatrix} 0 \\ 0 \\ l \end{bmatrix}. \quad (3.25)$$

Since a constant cross-section area is assumed, the following substitution applies

$$dA = D_R dl, \quad (3.26)$$

where D_R denotes the diameter of the rod. Substituting (3.26) and (3.25) into (3.24) the drag torque of the rod can be found by integrating

$$\boldsymbol{\tau}_{d,R} = \int_0^{L_R} \mathbf{l}_R \times d\mathbf{F}_{d,R} \quad (3.27)$$

over the total length of the rod L_R . Solving (3.27) leads to the drag torque defined in the coordinate frame of the rod as

$$\boldsymbol{\tau}_{d,R} = \frac{1}{2}\rho C_{d,R} D_R \frac{(L_R)^4}{4} \begin{bmatrix} |\dot{\varphi}| \dot{\varphi} \\ |\cos(\varphi) \dot{\theta}| \cos(\varphi) \dot{\theta} \\ 0 \end{bmatrix}. \quad (3.28)$$

Radiation Force

The radiation force of the buoy is taken into account using the radiation model outlined in Section 2.2.2. The continuous state space model of the radiation force due to the linear velocities of the buoy follows to

$$\dot{\mathbf{x}}_r = \mathbf{A}_r \mathbf{x}_r + \mathbf{B}_r \mathbf{v}_I^{\text{B},cb} \quad (3.29a)$$

$$\mathbf{F}_{r,B} = \mathbf{C}_r \mathbf{x}_r, \quad (3.29b)$$

with the state vector

$$\mathbf{x}_r = \begin{bmatrix} \mathbf{x}_{r,x} \\ \mathbf{x}_{r,y} \\ \mathbf{x}_{r,z} \end{bmatrix}, \quad (3.30)$$

and the matrices of the state space model

$$\mathbf{A}_r = \begin{bmatrix} \mathbf{A}_{r,x} & \mathbf{0} & \mathbf{0} \\ \mathbf{0} & \mathbf{A}_{r,y} & \mathbf{0} \\ \mathbf{0} & \mathbf{0} & \mathbf{A}_{r,z} \end{bmatrix}, \mathbf{B}_r = \begin{bmatrix} \mathbf{B}_{r,x} & \mathbf{0} & \mathbf{0} \\ \mathbf{0} & \mathbf{B}_{r,y} & \mathbf{0} \\ \mathbf{0} & \mathbf{0} & \mathbf{B}_{r,z} \end{bmatrix}, \quad (3.31)$$

$$\mathbf{C}_r = \begin{bmatrix} \mathbf{c}_{r,x}^T & \mathbf{0} & \mathbf{0} \\ \mathbf{0} & \mathbf{c}_{r,y}^T & \mathbf{0} \\ \mathbf{0} & \mathbf{0} & \mathbf{c}_{r,z}^T \end{bmatrix}.$$

Excitation Force

For the excitation force of the buoy, unidirectional waves are assumed and the direction of the incoming wave is considered to be known. The force acting on the buoy is generated by waves traveling in the positive x -direction (surge). Using (2.15), the modified force of the buoy in the inertial frame is given as

$$\check{\mathbf{F}}_{e,B} = \mathbf{f}_e(\zeta, V_{sub,B}, \mathbf{F}_e) \quad \text{with} \quad \mathbf{F}_e = \begin{bmatrix} F_{e,x} \\ 0 \\ F_{e,z} \end{bmatrix}, \quad (3.32)$$

and the nonlinear correction $\mathbf{f}_e(\cdot)$.

Machinery Force

The forces inside the buoy are referred to as the machinery force and comprise the force of the WaveSpring F_{wsp} , the force of the pretension cylinder F_{ptc} , and the transmission force F_{trans} , originating from the torque of the generator. In addition, for modeling the latching mechanism of the WEC, which locks and unlocks the motion of the buoy, the latching force F_{latch} is introduced. The forces add up to the machinery force

$$F_m = F_{wsp} - (F_{ptc} + F_{ptc,0}) + F_{trans} - F_{latch}, \quad (3.33)$$

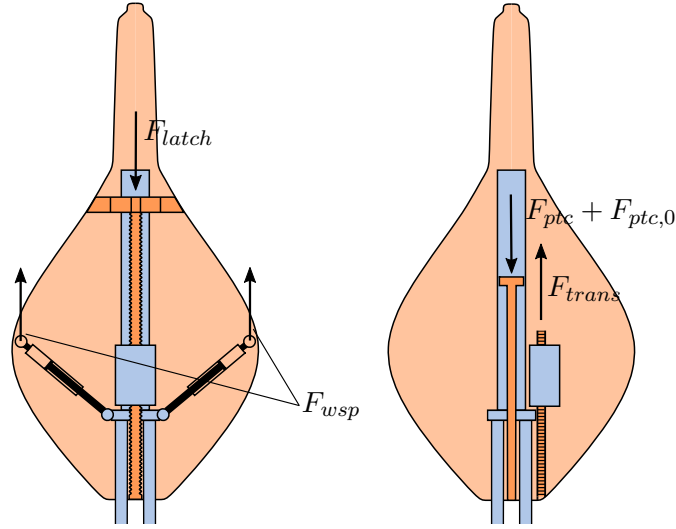


Figure 3.3: Machinery force components acting on the buoy

with $F_{ptc,0}$ being the constant pretension force. Figure 3.3 shows the machinery force components acting along the generalized coordinate s_{rack} . The behavior of the WaveSpring and pretension cylinder are modeled together using a nonlinear spring and nonlinear damping force. The forces can be written as

$$F_{wsp} - F_{ptc} = k_s(s_{rack})s_{rack} + F_f(\dot{s}_{rack}, s_{rack}), \quad (3.34)$$

where $k_s(\cdot)$ is the nonlinear stiffness and $F_f(\cdot)$ is the nonlinear friction of the system. Both functions are described by a polynomial. With the generator torque denoted as τ_{gen} , the transmission force calculates to

$$F_{trans} = \frac{u_{gbx}}{r_{pin}} \tau_{gen}. \quad (3.35)$$

The force during latching is modeled with the linear damper

$$F_c = c\dot{s}_{rack}, \quad (3.36)$$

where c is the damping constant. The constant c is approximated using W2W simulations. The latching mechanism is initiated by the binary latching state x_{latch} . To avoid applying a step in the input signal, the latching state is filtered by a second order system. The filtered latching state u_{latch} will be used as input for the WEC model. Thus, the latching force results in

$$F_{latch} = u_{latch} F_c. \quad (3.37)$$

With the constant pretension cylinder force $F_{ptc,0}$, the equilibrium position of the WEC is defined as

$$F_{ptc,0} = V_{B,0}\rho g - m_B g, \quad (3.38)$$

where $V_{B,0}$ is calculated using (3.19) with $\zeta = 0$ and $z_I^B = d_{mwI}$. Using the geometric Jacobians (3.9) and (3.10), the generalized forces are calculated as

$$\begin{aligned} \mathbf{f}_q = & \sum_{i \in \mathcal{B}} \left((\mathbf{J}_v)_I^{i,cg} \right)^T \mathbf{F}_{g,i} + \left((\mathbf{J}_v)_I^{i,cb} \right)^T \mathbf{F}_{b,i} \\ & + \left((\mathbf{J}_v)_I^{S,cb} \right)^T (\mathbf{F}_{d,S}) + \left((\mathbf{J}_\omega)_I^i \right)^T (\mathbf{R}_I^R \boldsymbol{\tau}_{d,R}) \\ & + \left((\mathbf{J}_v)_I^{B,cb} \right)^T (\mathbf{F}_{d,B} + \mathbf{F}_{r,B} + \check{\mathbf{F}}_{e,B}) + \begin{bmatrix} F_m \\ 0 \\ 0 \end{bmatrix}. \end{aligned} \quad (3.39)$$

By substituting (3.39) into (3.16) and rearranging the equations of motion, the rigid-body system can now be expressed as a set of first-order differential equations with

$$\frac{d}{dt} \begin{bmatrix} \mathbf{q} \\ \dot{\mathbf{q}} \end{bmatrix} = \begin{bmatrix} \dot{\mathbf{q}} \\ \mathbf{D}(\mathbf{q})^{-1} (-\mathbf{C}(\mathbf{q}, \dot{\mathbf{q}}) \dot{\mathbf{q}} + \mathbf{f}_q) \end{bmatrix}. \quad (3.40)$$

Combining (3.40) with the radiation model (3.29) yields the overall WEC model resulting in

$$\frac{d}{dt} \begin{bmatrix} \mathbf{q} \\ \dot{\mathbf{q}} \\ \mathbf{x}_r \end{bmatrix} = \begin{bmatrix} \dot{\mathbf{q}} \\ \mathbf{D}(\mathbf{q})^{-1} (-\mathbf{C}(\mathbf{q}, \dot{\mathbf{q}}) \dot{\mathbf{q}} + \mathbf{f}_q(\mathbf{q}, \dot{\mathbf{q}}, \mathbf{x}_r, \mathbf{u}, \zeta, \mathbf{F}_e)) \\ \mathbf{A}_r \mathbf{x}_r + \mathbf{B}_r \mathbf{v}_I^{B,cb} \end{bmatrix}, \quad (3.41)$$

with the control input

$$\mathbf{u} = \begin{bmatrix} \tau_{gen} & u_{latch} \end{bmatrix}^T. \quad (3.42)$$

The wave elevation ζ and the excitation force \mathbf{F}_e are treated as exogenous inputs in this formulation.

3.1.5 Model Simplification

The derived WEC model is used in the subsequent chapter to design a state observer. Hence, it makes sense to further simplify it in order to reduce the computational effort without significantly limiting the accuracy. In the following, approximations are made to simplify the nonlinear model (3.40). Due to the small deflection of the WEC, trigonometric functions are approximated using the small-angle approximation. Consequently, the cosine of a value is approximated as one, and the sine is approximated as the value itself. Furthermore, the angular velocities in roll and pitch are small enough that some quadratic coupling terms, which are present in the matrix $\mathbf{C}(\mathbf{q}, \dot{\mathbf{q}})$, can be neglected. Analyzing the product $\mathbf{C}(\mathbf{q}, \dot{\mathbf{q}}) \dot{\mathbf{q}}$ under irregular sea states, it is found that the coupling terms with the rack velocity \dot{s}_{rack} are dominant, so that Coriolis and centrifugal terms for roll and pitch are neglected. The reduced matrix results in

$$\mathbf{C}(\mathbf{q}, \dot{\mathbf{q}}) \approx \begin{bmatrix} 0 & 0 & 0 \\ c_{21}(\mathbf{q}, \dot{\varphi}) & c_{22}(\mathbf{q}, \dot{s}_{rack}) & 0 \\ c_{31}(\mathbf{q}, \dot{\theta}) & 0 & c_{32}(\mathbf{q}, \dot{s}_{rack}) \end{bmatrix}. \quad (3.43)$$

Recall that the rod is treated as a separate rigid body. Due to its low center of buoyancy and gravity, and its small cross-section area, it is assumed that it has little influence. The rod is therefore also neglected in the simplified model. To verify the derived 3-degree-of-freedom (3DoF) model (3.40) and the simplified model with the approximations just mentioned, they are compared with W2W simulations. Thereby, the states of both models are initialized with the states of the W2W model. The models are then simulated in an open loop alongside the W2W model for a period of time under irregular sea states. Figure 3.4 shows such a simulation result for the sea state with the highest probability of occurrence. The initial time was set to 540 seconds to capture the period when the roll and pitch angles have significant magnitudes. The 3DoF model follows the W2W model covering the relevant properties in the states. In addition, the reduced model differs only slightly from the 3DoF model, which shows the validity of the approximations made.

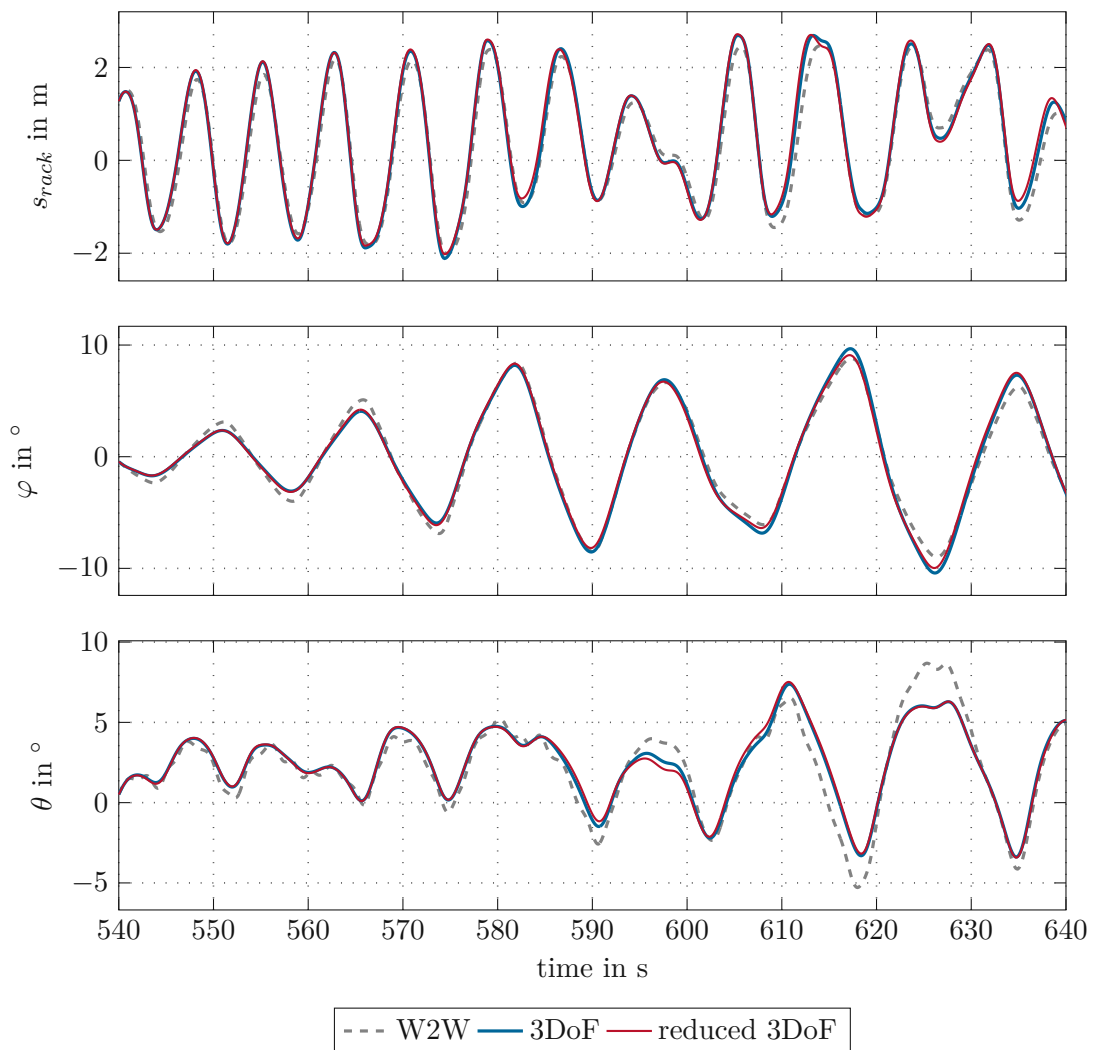


Figure 3.4: Open loop model comparison under irregular sea state ($H_s = 1.75\text{m}$, $T_e = 7\text{s}$).

3.2 Oscillator Model

The current approach of the company for estimating the wave elevation of an irregular wave is based on an oscillator model using n_o harmonic oscillators with constant frequencies. This model is adopted and briefly presented in the following. Using (2.6), the state space representation of the oscillator model using the n_o constant frequencies follows to

$$\dot{\mathbf{x}}_\eta = \mathbf{A}_\eta \mathbf{x}_\eta, \quad (3.44)$$

with the state vector

$$\mathbf{x}_\eta = \begin{bmatrix} \eta_1 \\ \vdots \\ \eta_{n_o} \\ \dot{\eta}_1 \\ \vdots \\ \dot{\eta}_{n_o} \end{bmatrix}, \quad (3.45)$$

and the dynamic matrix

$$\mathbf{A}_\eta = \begin{bmatrix} \mathbf{0} & \mathbf{I} \\ \mathbf{\Omega} & \mathbf{0} \end{bmatrix}, \quad \text{with} \quad \mathbf{\Omega} = \begin{bmatrix} -\omega_1^2 & 0 & \dots & 0 \\ 0 & -\omega_2^2 & \dots & 0 \\ \vdots & \vdots & \ddots & \vdots \\ 0 & 0 & \dots & -\omega_{n_o}^2 \end{bmatrix}. \quad (3.46)$$

An approximation for wave elevation of an irregular wave is defined by

$$\zeta = \sum_{i=1}^{n_o} \eta_i = \mathbf{c}_\eta^T \mathbf{x}_\eta. \quad (3.47)$$

Next, the relation between the excitation force and the oscillator model is determined. Considering that the formulation in (2.9) for the j^{th} component of the excitation force vector can be approximated using the oscillator states with

$$F_{e,j} \approx \sum_{i=1}^{n_o} \begin{bmatrix} a_{i,j} & b_{i,j} \end{bmatrix} \begin{bmatrix} \eta_i \\ \dot{\eta}_i \end{bmatrix}, \quad (3.48)$$

the coefficients $a_{i,j}$ and $b_{i,j}$ can be determined through a coefficient comparison between (2.9) and (3.48). Hence, the excitation force can be written as

$$\mathbf{F}_e = \begin{bmatrix} F_{e,x} \\ 0 \\ F_{e,z} \end{bmatrix} \approx \underbrace{\begin{bmatrix} \mathbf{c}_{e,x}^T \\ 0 \\ \mathbf{c}_{e,z}^T \end{bmatrix}}_{\mathbf{C}_e} \mathbf{x}_\eta, \quad (3.49)$$

with

$$\mathbf{c}_{e,j}^T = [a_{1,j} \dots a_{n_o,j} \ b_{1,j} \dots b_{n_o,j}], \quad j \in \{x, z\}. \quad (3.50)$$

3.3 Sensor Models

In the following, the sensor models for the sensors presented in Section 2.4 are derived.

3.3.1 Encoder

The encoder is mounted at the pinion and can measure N discrete positions per revolution. Consequently, the model for the encoder position s_{enc} with the pre-set value $s_{enc,0}$ of the encoder can simply be formulated as

$$s_{enc} = \frac{N}{2\pi r_{pin}} s_{rack} + s_{enc,0}. \quad (3.51)$$

Note that (3.51) does not yet consider the quantization of the encoder. In the simulated sensor signal, the quantization error of the encoder is taken into account by rounding s_{enc} to the nearest integer.

3.3.2 Pressure Sensor

The pressure sensor measures the hydrostatic and hydrodynamic pressure at the depth z_p . As the WEC model is considered a rigid body system, the sensor's position in the water remains constant relative to the slide's coordinate frame. It can be defined as $\mathbf{p}_S^{S,P} = [0 \ 0 \ z_S^{S,P}]^T$. The position with respect to the inertial frame, denoted as $\mathbf{p}_I^{S,P}$, can be obtained as demonstrated in Section 3.1.2. The z -position relative to the mean water level follows to

$$z_p = \mathbf{e}_z^T \mathbf{p}_I^{S,P} - d_{mwl}. \quad (3.52)$$

The pressure at this position can be determined using the Bernoulli equation (2.2). Adding the constant atmospheric pressure p_{atm} , the overall pressure obtained at the position z_p results in

$$p = \underbrace{-\rho \frac{\partial}{\partial t} \Phi}_{p_{hyd}} - \underbrace{\rho g z_p}_{p_{hyd}} + p_{atm}, \quad (3.53)$$

with the hydrodynamic pressure p_{hyd} and the hydrostatic pressure p_{hyd} . By using the solution for the velocity potential function Φ (2.4) together with the dispersion relationship (2.5), the hydrodynamic pressure can be expressed as a linear combination of regular wave components. To be able to use the sensor model in the estimation process, the hydrodynamic pressure is approximated using the wave components of the harmonic oscillator model. This results in

$$-\rho \frac{\partial}{\partial t} \Phi \approx \rho g \sum_{i=1}^{n_o} \frac{\cosh(k(\omega_i)(d + z_{p,0}))}{\cosh(k(\omega_i)d)} \eta_i = \mathbf{c}_p^T \mathbf{x}_\eta, \quad (3.54)$$

where z_p is replaced with the sensor position in the equilibrium of the WEC

$$z_{p,0} = d_S + z_S^{S,P} - d_{mwl}. \quad (3.55)$$

The constant d_S refers to the distance from the universal joint to the origin of the slide coordinate frame (see Figure 3.2). Since (3.54) is insensitive to changes in the sensor

position, the resulting error due to the use of a constant sensor position remains within the measurement uncertainty of the sensor. This was also confirmed by simulations. Additionally, this approximation results in the constant output vector \mathbf{c}_p^T , which also considerably simplifies the calculation of its linearization later on. The model for the measured pressure p can be written as

$$p = \mathbf{c}_p^T \mathbf{x}_\eta - \rho g \left(\mathbf{e}_z^T \mathbf{p}_I^{S,P} - d_{mwl} \right) + p_{atm} \quad (3.56)$$

3.3.3 Inertial Measurement Unit

The measurements utilized from the IMUs include acceleration, as well as the estimates of angular velocity and attitude, obtained through their internal extended Kalman filter. The IMU fixed to the slide will be denoted as S, IMU and the IMU mounted on the buoy as B, IMU. Furthermore, their position in the body-fixed coordinate frame is determined by the constant position vector $\mathbf{p}_i^{i,IMU}$ and the constant rotation matrix $\mathbf{R}_i^{i,IMU}$ with $i \in \mathcal{I} = \{S, B\}$.

The measured acceleration comprises both the acceleration due to gravity and the sensor's acceleration. To derive the acceleration of the IMUs, the position vectors are first transformed into the inertial frame, where the second time derivative of the position yields the acceleration in the inertial frame $\ddot{\mathbf{p}}_I^{i,IMU}$. The gravitational acceleration in the inertial frame is given as $\mathbf{g}_I = [0 \ 0 \ -g]^T$. Since the measured acceleration $\mathbf{a}_{i,IMU}$ is given in the coordinate frame of the IMUs, the transformation of $\ddot{\mathbf{p}}_I^{i,IMU}$ and \mathbf{g}_I is obtained by using the rotation matrix

$$\mathbf{R}_{i,IMU}^I = \left(\mathbf{R}_I^i \mathbf{R}_i^{i,IMU} \right)^T, \quad i \in \mathcal{I}. \quad (3.57)$$

The model for the measured acceleration follows to

$$\mathbf{a}_{i,IMU} = \mathbf{R}_{i,IMU}^I \left(\ddot{\mathbf{p}}_I^{i,IMU} + \mathbf{g}_I \right), \quad i \in \mathcal{I}. \quad (3.58)$$

The angular velocities $\boldsymbol{\omega}_{i,IMU}$ of the IMUs are obtained by using the angular velocities of the slide and buoy from (3.8) and rotating them with $\mathbf{R}_{i,IMU}^I$ into the IMUs coordinate frame. As the internal extended Kalman filters already compensate for the gyro bias, it can be assumed that the remaining uncertainty can later be modeled by adding zero-mean measurement noise. The model for the angular velocities results in

$$\boldsymbol{\omega}_{i,IMU} = \mathbf{R}_{i,IMU}^I \boldsymbol{\omega}_I^i, \quad i \in \mathcal{I}. \quad (3.59)$$

Because of the alignment of the IMUs' coordinate axes with those of the buoy and slide, in addition to the disregard of the yaw angle as a degree of freedom in the WEC model, the yaw rate in $\boldsymbol{\omega}_{i,IMU}$ remains close to zero. However, the simulated yaw rate of the W2W model is significant, which leads to a large error between the two models. Consequently, the yaw rate will be disregarded as measurement. The same applies to the model of the attitude $\boldsymbol{\Theta}_{i,IMU}$, where only the roll and pitch angles ($\varphi_{i,IMU}$ and $\theta_{i,IMU}$) are used. The attitude estimates of the IMUs are given with reference to the North East Down (NED) frame. Assuming that the rotation between the inertial frame and the NED frame,

denoted as $\mathbf{R}_{\text{NED}}^{\text{I}}$, is known, the orientation of the IMUs coordinate frames with respect to the NED frame is given as

$$\mathbf{R}_{\text{NED}}^{i,\text{IMU}} = \mathbf{R}_{\text{NED}}^{\text{I}} \mathbf{R}_{\text{I}}^i \mathbf{R}_i^{i,\text{IMU}}, \quad i \in \mathcal{I}. \quad (3.60)$$

According to the datasheet of the IMUs, the attitude is given as a 3,2,1 Euler angle sequence. Hence, the roll and pitch angles of the IMUs can be extracted from (3.60) [52], resulting in

$$\varphi_{i,\text{IMU}} = \arctan \left(\frac{\mathbf{R}_{\text{NED}}^{i,\text{IMU}}(3,2)}{\mathbf{R}_{\text{NED}}^{i,\text{IMU}}(3,3)} \right), \quad (3.61a)$$

$$\theta_{i,\text{IMU}} = \arcsin \left(-\mathbf{R}_{\text{NED}}^{i,\text{IMU}}(3,1) \right), \quad (3.61b)$$

with $i \in \mathcal{I}$. The model for the attitude follows to

$$\Theta_{i,\text{IMU}} = \begin{bmatrix} \varphi_{i,\text{IMU}} \\ \theta_{i,\text{IMU}} \end{bmatrix}, \quad i \in \mathcal{I}. \quad (3.62)$$

4 Estimation

In this chapter, an observer for the estimation task is designed on the basis of the derived mathematical models. The basics of the Extended Kalman Filter and the associated estimation algorithm are briefly presented. After tuning the observer, the quality of the estimation is studied and compared with the current estimation approach. Further, the robustness against sensor failures is evaluated and the significance of using a 3DoF WEC model is investigated.

4.1 Dynamic System

Before designing an observer, the derived models are used to formulate a nonlinear continuous-time dynamic system, comprising a state equation and an output equation. This dynamic system forms the basis for the observer which is used to estimate the wave elevation and the excitation force in the surge and heave direction. The state equation is obtained by combining the WEC model (3.41), along with the approximations detailed in Section 3.1.5, and the harmonic oscillator model (3.44). The state equation is formulated as

$$\frac{d}{dt}\mathbf{x} = \mathbf{f}(\mathbf{x}, \mathbf{u}) = \frac{d}{dt} \begin{bmatrix} \mathbf{q} \\ \dot{\mathbf{q}} \\ \mathbf{x}_r \\ \mathbf{x}_\eta \end{bmatrix} = \begin{bmatrix} \dot{\mathbf{q}} \\ \mathbf{D}(\mathbf{q})^{-1}(-\mathbf{C}(\mathbf{q}, \dot{\mathbf{q}})\dot{\mathbf{q}} + \mathbf{f}_q(\mathbf{x}, \mathbf{u})) \\ \mathbf{A}_r \mathbf{x}_r + \mathbf{B}_r \mathbf{v}_1^{\mathbf{B}, cb} \\ \mathbf{A}_\eta \mathbf{x}_\eta \end{bmatrix}, \quad (4.1)$$

where the wave elevation and excitation force, which were exogenous inputs to the WEC model, can now be calculated from the states of the harmonic oscillator model. The output equation can be easily derived from the sensor models organized in the output vector \mathbf{y} with

$$\mathbf{y} = \mathbf{h}(\mathbf{x}, \mathbf{u}) = \begin{bmatrix} s_{enc}(s_{rack}) \\ p(\mathbf{x}_\eta, \varphi, \theta) \\ \Theta_{\mathbf{S}, \text{IMU}}(\varphi, \theta) \\ \omega_{\mathbf{S}, \text{IMU}}(\varphi, \dot{\varphi}, \dot{\theta}) \\ \mathbf{a}_{\mathbf{S}, \text{IMU}}(\mathbf{x}, \mathbf{u}) \\ \Theta_{\mathbf{B}, \text{IMU}}(\varphi, \theta) \\ \omega_{\mathbf{B}, \text{IMU}}(\varphi, \dot{\varphi}, \dot{\theta}) \\ \mathbf{a}_{\mathbf{B}, \text{IMU}}(\mathbf{x}, \mathbf{u}) \end{bmatrix} \quad (4.2)$$

4.2 Extended Kalman Filter

A common approach for observing the state of dynamic systems is the application of the Kalman filter (KF) [53]. The dynamic system described in Section 4.1 is non-linear but given as continuously differentiable functions. As a first choice, it is therefore reasonable to use the extended Kalman filter (EKF) as observer. To implement the EKF on a real-time computing unit, it is necessary to discretize the dynamic system. In this work, the discrete-time dynamics are obtained by integrating the state equation (4.1) in time using the explicit Euler method. The corresponding discretized state equation results in

$$\mathbf{x}_{k+1} = \mathbf{x}_k + \mathbf{f}(\mathbf{x}_k, \mathbf{u}_k)T_s = \mathbf{F}_k(\mathbf{x}_k, \mathbf{u}_k), \quad (4.3)$$

with $k = 1, 2, \dots$ and the constant sampling time T_s . The output equation of the discrete system reads as

$$\mathbf{y}_k = \mathbf{h}(\mathbf{x}_k, \mathbf{u}_k). \quad (4.4)$$

For the observer design, the process noise \mathbf{w}_k and the measurement noise \mathbf{v}_k need to be considered and are chosen additive to the above formulations, i.e.

$$\mathbf{x}_{k+1} = \mathbf{F}_k(\mathbf{x}_k, \mathbf{u}_k) + \mathbf{w}_k, \quad (4.5a)$$

$$\mathbf{y}_k = \mathbf{h}(\mathbf{x}_k, \mathbf{u}_k) + \mathbf{v}_k, \quad (4.5b)$$

with properties for the stochastic variables [53]

$$\mathbf{E}(\mathbf{v}_k) = \mathbf{0} \quad \mathbf{E}(\mathbf{v}_k \mathbf{v}_j^T) = \mathbf{R} \delta_{kj} \quad (4.6a)$$

$$\mathbf{E}(\mathbf{w}_k) = \mathbf{0} \quad \mathbf{E}(\mathbf{w}_k \mathbf{w}_j^T) = \mathbf{Q} \delta_{kj} \quad (4.6b)$$

$$\mathbf{E}(\mathbf{w}_k \mathbf{v}_j^T) = \mathbf{0} \quad (4.6c)$$

where $\mathbf{E}(\cdot)$ denotes the expected value and δ_{kj} is the Kronecker delta function with $\delta_{kj} = 1$ if $k = j$ and $\delta_{kj} = 0$ if $k \neq j$. Furthermore, \mathbf{Q} and \mathbf{R} denote the constant positive definite covariance matrices of the process noise and measurement noise, respectively. The choice of these two matrices is discussed in the subsequent section. In the following, the estimation procedure of the EKF is briefly outlined.

Let $\hat{\mathbf{x}}_k^-$ and $\hat{\mathbf{x}}_k^+$ denote the estimates of the state before and after considering the measurement \mathbf{y}_k , respectively. They are also referred to as a priori and a posteriori estimate. The state estimation update then follows to [53]

$$\hat{\mathbf{x}}_k^+ = \hat{\mathbf{x}}_k^- + \hat{\mathbf{L}}_k \left(\mathbf{y}_k - \mathbf{h}_k(\hat{\mathbf{x}}_k^-, \mathbf{u}_k) \right), \quad (4.7)$$

with the Kalman gain

$$\hat{\mathbf{L}}_k = \mathbf{P}_k \mathbf{C}_k^T \left(\mathbf{C}_k \mathbf{P}_k \mathbf{C}_k^T + \mathbf{R} \right)^{-1}. \quad (4.8)$$

In (4.8), \mathbf{C}_k is the linearized output equation given as

$$\mathbf{C}_k = \left. \frac{\partial}{\partial \mathbf{x}_k} \mathbf{h}_k(\mathbf{x}_k, \mathbf{u}_k) \right|_{\mathbf{x}_k = \hat{\mathbf{x}}_k^-, \mathbf{u}_k = \mathbf{u}_k}, \quad (4.9)$$

and \mathbf{P}_k is the covariance matrix of the estimation error with \mathbf{P}_0 being the covariance of the initial estimate $\hat{\mathbf{x}}_0^-$. Its iteration is calculated as [53]

$$\mathbf{P}_{k+1} = \Phi_k \mathbf{P}_k \Phi_k^T + \mathbf{Q} + \Phi_k \hat{\mathbf{L}}_k \mathbf{C}_k \mathbf{P}_k \Phi_k^T, \quad (4.10)$$

in which Φ_k denotes the dynamic matrix of the system resulting in

$$\Phi_k = \left. \frac{\partial}{\partial \mathbf{x}_k} \mathbf{F}_k(\mathbf{x}_k, \mathbf{u}_k) \right|_{\mathbf{x}_k = \hat{\mathbf{x}}_k^+, \mathbf{u}_k = \mathbf{u}_k}, \quad (4.11)$$

with

$$\frac{\partial}{\partial \mathbf{x}_k} \mathbf{F}_k(\mathbf{x}_k, \mathbf{u}_k) = \mathbf{I} + \frac{\partial}{\partial \mathbf{x}_k} \mathbf{f}(\mathbf{x}_k, \mathbf{u}_k) T_s. \quad (4.12)$$

In (4.12), \mathbf{I} refers to the identity matrix. The time prediction step of the state vector gives the a priori estimate with

$$\hat{\mathbf{x}}_{k+1}^- = \mathbf{F}_k(\hat{\mathbf{x}}_k^+, \mathbf{u}_k). \quad (4.13)$$

The estimated wave elevation $\hat{\zeta}_k$ and excitation force $\hat{\mathbf{F}}_{e,k}$ are extracted from the state estimation update (4.7) using the relations (3.47) and (3.49)

$$\hat{\zeta}_k = \mathbf{c}_\eta^T \hat{\mathbf{x}}_{\eta,k}^+ \quad (4.14a)$$

$$\hat{\mathbf{F}}_{e,k} = \mathbf{C}_e \hat{\mathbf{x}}_{\eta,k}^+ = \begin{bmatrix} \hat{F}_{e,x,k} \\ 0 \\ \hat{F}_{e,z,k} \end{bmatrix} \quad (4.14b)$$

4.3 Tuning

The covariance matrices \mathbf{R} and \mathbf{Q} account for uncertainties in the measurements and un-modeled disturbances. The choice and ratio between the two matrices determine which and how much the measurements are trusted compared to the model. Thus, a desired behavior in the state estimation can be achieved. The purpose in this case is to tune the two matrices to achieve a certain performance in estimating wave elevation and excitation force. Since it is assumed that the sensors and the process noise are uncorrelated, both covariance matrices are taken as diagonal matrices.

4.3.1 Measurement Noise

The entries of \mathbf{R} are chosen based on the sensor properties derived from the data sheets or taken from measurements. However, according to W2W simulations, oscillations of the buoy and slide can occur due to the flexibility of the mooring rod, which are not captured by the 3DoF model. Yet, these oscillations are accurately detected by the IMUs in the simulations. As a result, this would negatively affect the estimation accuracy of the wave elevation and excitation force. To address this issue, the corresponding entries in the main diagonal of the covariance matrix \mathbf{R} are increased for the IMU measurements, i.e., the measurements are considered less reliable to reject these oscillations. The corresponding entries refer to the third to eighth row of the output vector (4.2).

4.3.2 Process Noise

The covariance matrix of the process noise read as

$$\mathbf{Q} = \mathbb{E}(\mathbf{w}_k \mathbf{w}_k^T) = \text{diag}[\sigma_q^2, \sigma_v^2, \sigma_r^2, \sigma_\eta^2], \quad (4.15)$$

where σ_q^2 are the variances of the position states \mathbf{q} , σ_v^2 are the variances of the velocity states $\dot{\mathbf{q}}$, σ_r^2 are the variances of the radiation model, and σ_η^2 are the variances of the oscillator states \mathbf{x}_η . The variances of the velocity states are identified by simulating the 3DoF model in open loop next to the W2W model. The process noise is assumed to quantify the error between the states of the 3DoF model and the states of the W2W model. Therefore, the variances of the errors are calculated and used as variances in the \mathbf{Q} matrix. With the process noise of the position states, discretization errors caused by the integration method are considered. The values of σ_q^2 can therefore be assumed to be relatively small and are tuned based on simulations. Regarding the radiation model, a common approach is to exclude the radiation states from having a process noise variance. Instead un-modeled disturbances in the radiation force are accounted for in the velocity states [54]. In this case, σ_r^2 is used to account for discretization errors in the radiation model. Errors due to the radiation force are already considered in σ_v^2 due to the identification process. The variances of the oscillator states are chosen to be equal with

$$\sigma_\eta^2 = \sigma_\eta^2 [1, \dots, 1], \quad (4.16)$$

since individual tuning goes beyond the scope of this work. The variances σ_η^2 should be tuned so that the harmonic oscillators are capable of modeling the wave process as accurately as possible. For this purpose, an objective function is used, which quantifies the quality of the estimated wave elevation and excitation force. A common method for determining the quality of an estimated signal is to use the normalized root-mean-square accuracy (NRMSA) [15]. The NRMSA of a discrete-time signal x_k with the corresponding estimate \hat{x}_k is represented by

$$\text{NRMSA} = 1 - \sqrt{\frac{\sum_{k=1}^n (x_k - \hat{x}_k)^2}{\sum_{k=1}^n x_k^2}}, \quad (4.17)$$

with $\text{NRMSA} = 1$ being the highest achievable accuracy. Since the goal of the EKF is to provide an accurate estimate of both the wave elevation and the excitation force, the objective function based on (4.17) for a specific sea state s is written as

$$J_s = 1 - \sqrt{\frac{\sum_{k=N_s}^{L_s} (\mathbf{X}_k - \hat{\mathbf{X}}_k)^T (\mathbf{X}_k - \hat{\mathbf{X}}_k)}{\sum_{k=N_s}^{L_s} \mathbf{X}_k^T \mathbf{X}_k}}, \quad \mathbf{X}_k = \begin{bmatrix} \zeta_k \\ \mathbf{F}_{e,k} \end{bmatrix}, \quad (4.18)$$

where L_s denotes the entire samples in the simulation and N_s denotes the first sample for which the objective function is evaluated. N_s is used to avoid the time in which the EKF converges. The EKF is expected to perform properly across different sea states, thus the objective function is weighted with

$$J = \frac{1}{\sum_{s \in \mathcal{S}} P(s)} \sum_{s \in \mathcal{S}} P(s) J_s, \quad (4.19)$$

where $P(s)$ is the probability of occurrence for a certain sea state (see Figure 2.1), and \mathcal{S} denotes the set of sea states in tuned mode. Figure 4.1 shows the simulation result where the objective function (4.19) is evaluated over a range of process noise values σ_η^2 . A suitable value is defined by the local maximum of the objective function.

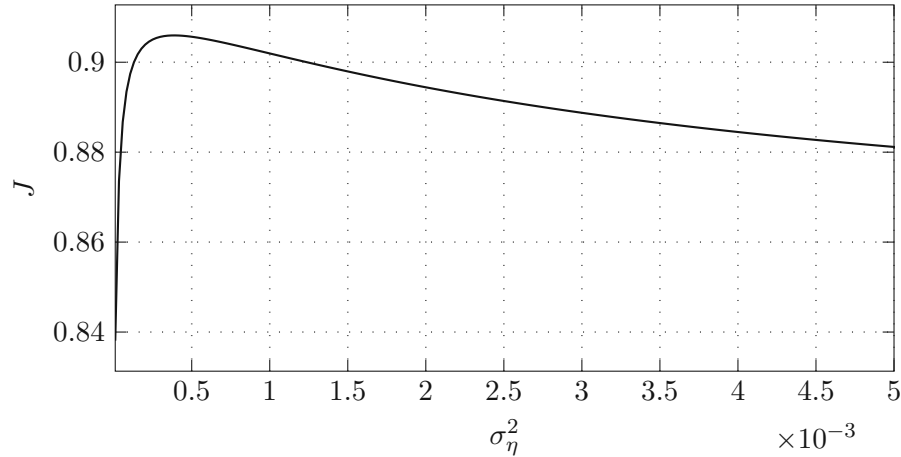


Figure 4.1: Tuning of process noise variance for the harmonic oscillator states

4.3.3 Initial Error Covariance

Another design decision of the EKF are its initial values \mathbf{P}_0 and $\hat{\mathbf{x}}_0^-$. If the initial state is not known, one usually sets

$$\hat{\mathbf{x}}_0^- = \mathbf{0} \quad (4.20a)$$

$$\mathbf{P}_0 = \alpha \mathbf{I}, \quad (4.20b)$$

with $\alpha \gg 1$ [53]. In this work, the measured states can be initialized with the sensor values. The corresponding entries in \mathbf{P}_0 are set to the variances of the sensor noise. The remaining values are tuned according to (4.20).

4.4 Results

The performance of the presented EKF is validated through W2W simulations. The estimated wave elevation and excitation force are compared with the corresponding values from the W2W model, which, as previously mentioned, are inputs to the simulation and serve as reference. In addition, the EKF is compared with the already existing observer: a linear Kalman filter that uses the pressure sensor signal and the harmonic oscillator model (3.44) to estimate the wave elevation and calculate the excitation force in surge and heave from it. Its dynamic system is given as

$$\dot{\mathbf{x}}_\eta = \mathbf{A}_\eta \mathbf{x}_\eta, \quad (4.21a)$$

$$y = p_{hyd} = \mathbf{c}_p^T \mathbf{x}_\eta. \quad (4.21b)$$

Since the oscillator model only represents the hydrodynamic pressure p_{hyd} , the pressure sensor signal must be additionally manipulated with this method. This includes a correction of the sensor position using the IMUs and a high-pass filter to eliminate hydrostatic pressure. It should also be noted that the W2W model assumes unidirectional waves. For the evaluation, it is assumed that the direction of the incoming wave is known. Consequently, only waves traveling in positive x -direction (surge) are considered. The evaluation is conducted under the sea states in tuned mode (see Figure 2.1), each with a simulation time of 1000s. Values from 100s on are used to avoid the transient behavior of the observers.

4.4.1 Assessment of EKF and Bias Compensation

During the evaluation of the EKF, it became evident that neglecting the pressure sensor as measurement leads to a significant mean value error in the estimates of the wave elevation and excitation force. Figure 4.2 shows this mean $\mu_{\hat{\zeta}}$ in the estimated wave elevation of the EKF $\hat{\zeta}$. The presence of the non-zero mean in this context can be attributed primarily

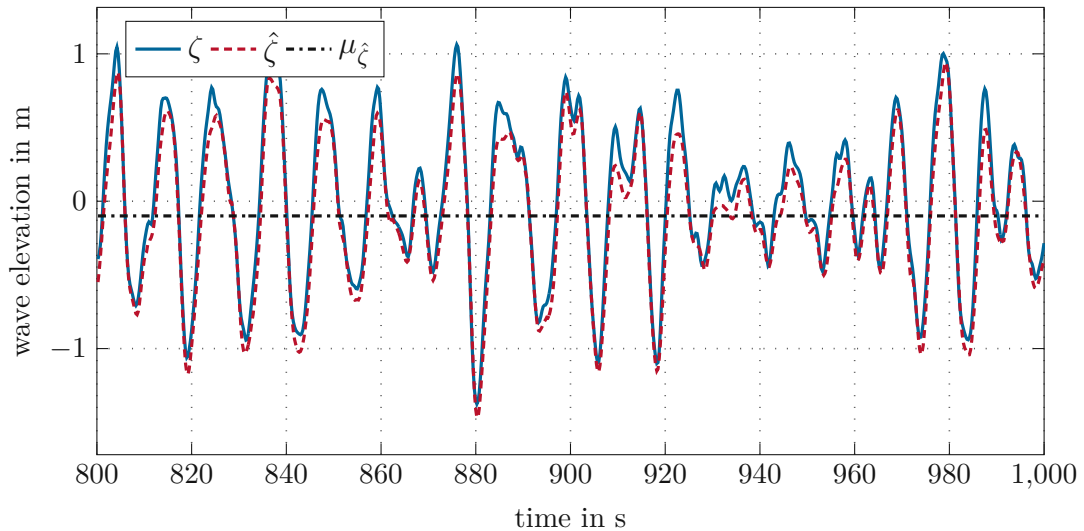


Figure 4.2: Estimated wave elevation of EKF without pressure measurement ($H_s = 1.75\text{m}$, $T_e = 10\text{s}$).

to non-zero means in the states like rack position or roll and pitch angle. To address this issue and reduce the bias in the estimates, the dynamic system (4.1) is augmented by the state η_0 , which represents a mean wave elevation. Its dynamic is characterized by a random walk model, suitable for capturing slowly changing quantities. Hence, the dynamic equation can be expressed as

$$\frac{d}{dt} \begin{bmatrix} \mathbf{x} \\ \eta_0 \end{bmatrix} = \dot{\mathbf{x}}^a = \begin{bmatrix} \mathbf{f}(\mathbf{x}^a, \mathbf{u}) \\ 0 \end{bmatrix}. \quad (4.22)$$

Since the state variable η_0 is intended to represent a mean wave elevation, it is necessary to include it in the expressions for both the wave elevation (3.47) and the excitation force (3.49). The wave elevation of the irregular wave is redefined as

$$\bar{\zeta} = \underbrace{\mathbf{c}_\eta^T \mathbf{x}_\eta}_{\zeta} + \eta_0, \quad (4.23)$$

The excitation force including the state η_0 reads as

$$\bar{\mathbf{F}}_e = \underbrace{\mathbf{C}_e \mathbf{x}_\eta}_{\mathbf{F}_e} + \begin{bmatrix} 0 \\ 0 \\ \rho g A_{wp} \end{bmatrix} \eta_0, \quad (4.24)$$

where A_{wp} is the water plane area of the buoy in the equilibrium position of the WEC, and the product $\rho g A_{wp}$ is the magnitude response of the excitation force in heave direction at zero frequency. As can be seen in (4.24), a mean wave elevation does not affect the excitation force in the surge direction. This is not surprising, as a constant sea level cannot cause lateral movement of the WEC. The variables ζ and \mathbf{F}_e from (4.23) and (4.24) describe the bias-free components of the wave elevation and excitation force, respectively, and are replaced by $\bar{\zeta}$ and $\bar{\mathbf{F}}_e$ in the mechanical model (3.41). With this approach, the mean values of the estimated wave elevation and excitation force according to (4.14) should be reduced. It may be recalled that the oscillator states \mathbf{x}_η are also used in the pressure sensor model (3.56). One might anticipate that η_0 is likewise incorporated into the output equation for the pressure sensor. However, as the state should represent a fictitious mean water level, the pressure sensor is not affected by this. Thus, it is not considered in the pressure sensor model.

In order to investigate the influence of the state η_0 , the distribution of the estimation errors is evaluated by means of their mean values and standard deviations. To enhance the comparability of the estimated quantities, the estimation errors are normalized. This involves dividing the estimation errors for each sea state by the difference between the maximum and minimum values of the corresponding reference variable. In addition, this normalization makes it possible to concatenate the normalized error signals across all considered sea states. Thus, an overall distribution of the estimation errors across the examined sea states is determined to quantify the effect of η_0 . Figure 4.3 shows the normalized distribution of estimation errors for both the EKF incorporating the state η_0 , and the EKF without the augmented state vector \mathbf{x} , cf. (4.22). The standard deviations and mean values for the estimated quantities are indicated with σ and μ . As can be observed, the mean value of the wave elevation and excitation force error in heave is reduced by a factor of approximately ten if η_0 is considered in the observer design. The associated standard deviations are marginally positively influenced as well. The changes in the standard deviation and the mean value for the error of the excitation force in the surge, on the other hand, are insignificant. Figure 4.3 illustrates the distribution of estimation errors when the pressure sensor is excluded as measurement in the EKFs, as significant mean value errors were observed in this scenario.

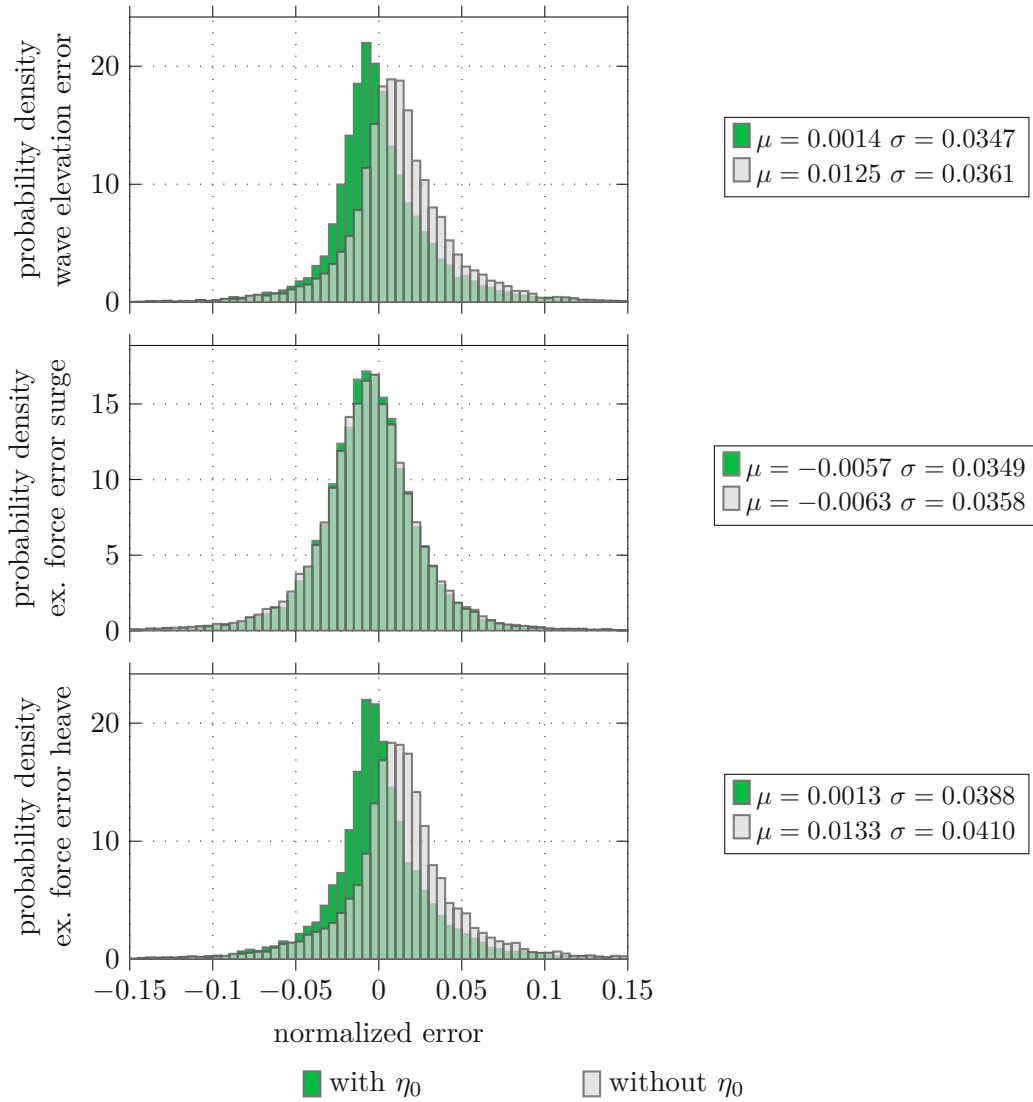


Figure 4.3: Impact of η_0 on the distribution of the estimation errors without pressure sensor

Figure 4.4 shows a similar comparison. In this case, however, the pressure sensor is included as measurement in order to determine the effects of η_0 again. When comparing the standard deviations and the mean values, it can be seen that the incorporation of η_0 also has a slightly positive influence on the overall quality of the estimates. As η_0 represents a fictitious mean wave elevation, these comparisons cannot be used to determine which mean values of the states are compensated for and to what extent. However, since considering η_0 has a positive influence on the estimates, it is used in the EKF design for further comparisons.

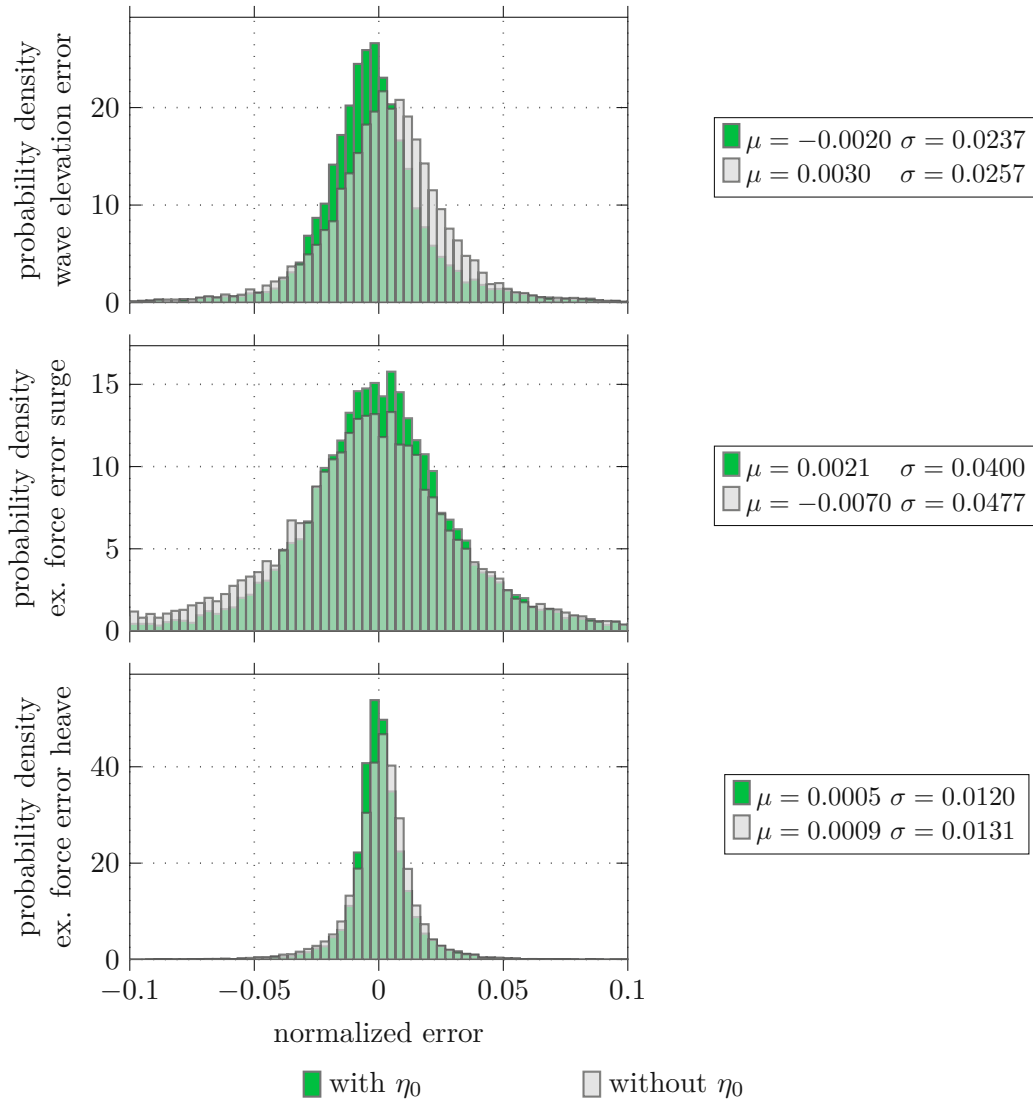


Figure 4.4: Impact of η_0 on the distribution of the estimation errors with pressure sensor

4.4.2 Comparison of EKF and Linear KF

It was verified with simulation that the linear KF based on (4.21) using n_o harmonic oscillators is able to accurately estimate the hydrodynamic pressure. Therefore, the accuracy of the wave elevation estimate primarily depends on the transfer behavior between the hydrodynamic pressure and wave elevation. Based on (3.54)

$$H_p(\omega) = \rho g \frac{\cosh(k(\omega)(d + z_{p,0}))}{\cosh(k(\omega)d)}. \quad (4.25)$$

holds. Figure 4.5 shows its magnitude response, indicating a low-pass characteristic at higher wave frequencies. Wave periods between 20s and 4s are particularly present in the sea states with a high probability of occurrence. However, the magnitudes in this range are already decreased by approximately -20dB , i.e. reduced to approx. 10%. Waves below 4s are hardly detected by the pressure sensor, but are of little importance for energy generation anyway. As a result, this low-pass characteristic is a main limiting factor for the estimation accuracy based on pressure measurements.

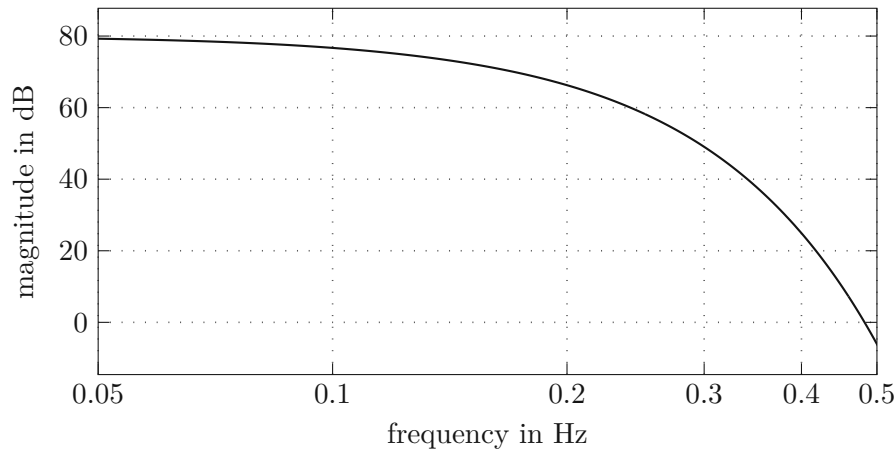


Figure 4.5: Magnitude response of $H_p(\omega)$

Time Series Comparison

Figure 4.6 shows a comparison for the estimated wave elevation and excitation force in both surge and heave of the linear KF and EKF. The corresponding input signals of the W2W model are shown as reference. Observing the estimation of the wave elevation, it is noticeable that higher frequency components are missing in the estimation, especially for the linear KF, resulting in underestimated amplitudes. This can be attributed to the low-pass characteristics described above. Although the EKF use the same n_o frequencies in the oscillator model as the linear KF, its amplitudes of the wave elevation are estimated more accurately. This could be explained by the error covariances of the higher frequency oscillator states being significantly reduced by the use of several independent measurements. A notable difference in estimates is also evident for the excitation force in the surge. In the

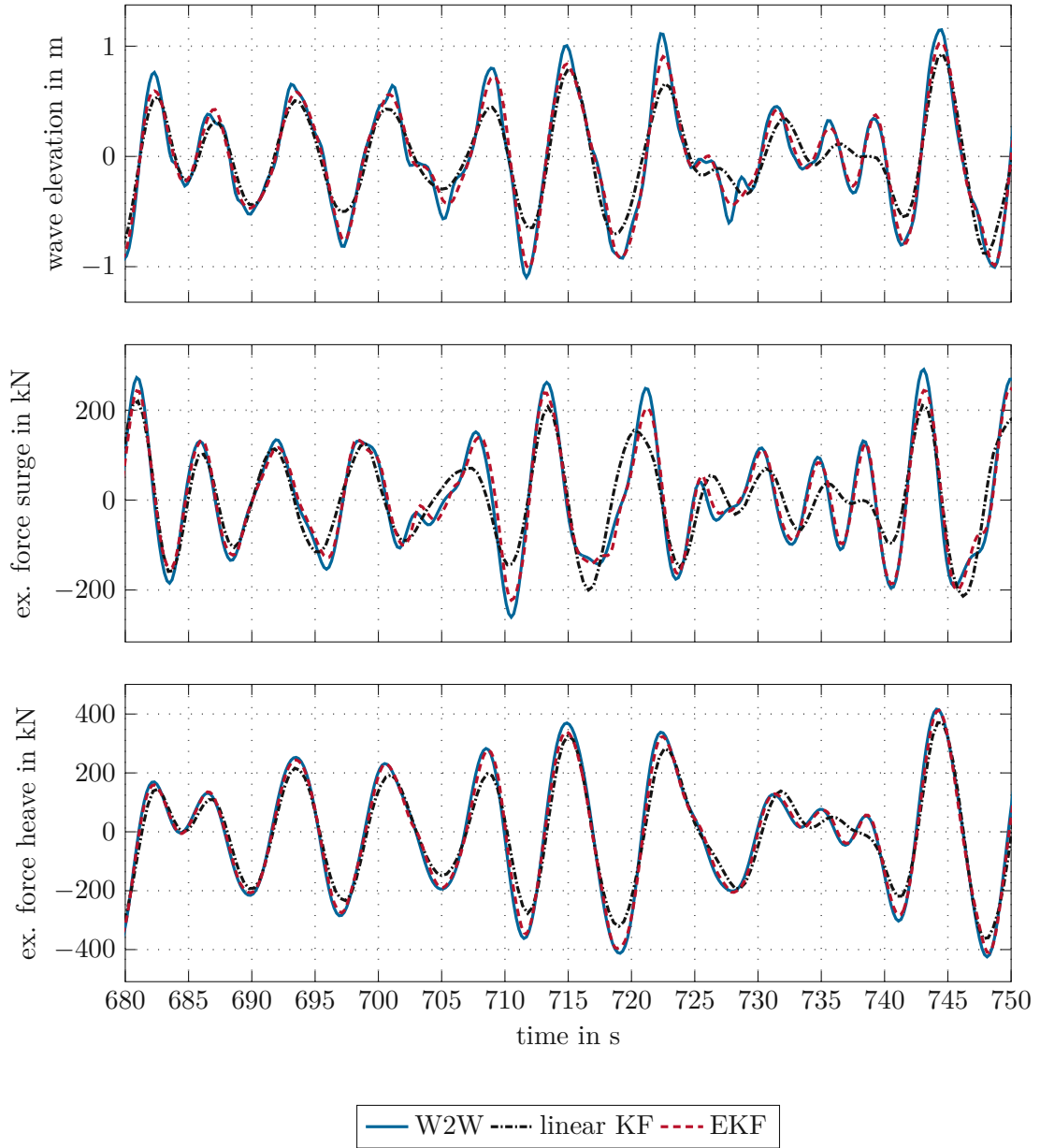


Figure 4.6: Time series comparison ($H_s = 1.75\text{m}$, $T_e = 7\text{s}$).

case of the linear KF, this force is computed from the estimated wave elevation. However, the accuracy is notably restricted which can be attributed to the transfer behavior of the wave elevation to the excitation force in surge. In the EKF, the mechanical model provides direct feedback on the excitation force in the surge leading to an improvement in the estimate. Figure 4.6 also shows that the estimation of the excitation force in heave with both the linear KF and the EKF appears to be more accurate compared to the other estimates. This can again be related to the transfer behavior. Similar to the pressure, the behavior of the wave elevation to the excitation force in heave exhibits a low-pass characteristic. Consequently, the pressure sensor signal represents the excitation force in heave more accurately than the wave elevation, resulting in a more precise estimation.

NRMSA Comparison

To evaluate the performance of the observers for each sea state in tuned mode, the NRMSA approach can be applied again. The NRMSA, as specified in (4.17), is used to calculate the quality of the estimated wave elevation and excitation force in surge and heave. Table 4.1 shows the results of the linear KF and EKF across the individual sea states. It is noticeable that with the linear Kalman filter, the NRMSA increases with increasing wave period T_e for the wave elevation estimate and the excitation force estimate in heave. However, this tendency barely exists for the excitation force estimation in the surge. As already indicated, this can be attributed to the transfer behavior between the wave elevation and excitation force in the surge. In the range of the oscillator frequencies, it exhibits a high-pass characteristic. Consequently, due to the low-pass characteristic of the estimated wave elevation of the linear KF, the excitation force in the surge can therefore only be calculated poorly. Low-pass characteristics have less influence with increasing wave period, thus improving the NRMSA of the wave elevation and excitation force in heave for the linear KF. A comparison of the NRMSA of the linear KF and the EKF for sea states with a high probability of occurrence ($T_e = 7\text{s}$ and $T_e = 10\text{s}$) shows that the EKF exceeds the linear KF for all three estimated quantities. However, as the wave period or significant wave height increases, the advantage of the EKF over the linear KF reduces. This discrepancy might arise from the simplifications made in the 3DoF model. It is particularly striking that the NRMSA of the EKF for the excitation force in surge is significantly reduced for $T_e = 16\text{s}$. However, due to the negligible probability of occurrence of these sea states, no further investigations were conducted to determine which effects are responsible for this loss of accuracy.

Estimation Error Distribution

When determining the quality of the estimation using the NRMSA, an error due to a possible non-zero mean is included in the assessment. As in Section 4.4.1, the mean value and the distribution of the estimation errors are therefore examined separately. Figure 4.7 shows the distribution of the normalized estimation errors for the linear KF and EKF, accumulated over the sea states in tuned mode. The mean values and standard deviations are given with μ and σ . The majority of the estimation errors of the EKF are distributed over a considerably smaller range with a standard deviation that is reduced significantly

T_e (s)	H_s (m)	Wave elevation		Ex. force surge		Ex. force heave	
		Linear KF	EKF	Linear KF	EKF	Linear KF	EKF
4	1	0.24	0.64	0.30	0.86	0.42	0.86
	1.75	0.23	0.63	0.30	0.82	0.42	0.84
7	1	0.62	0.87	0.51	0.87	0.78	0.94
	1.75	0.62	0.86	0.50	0.84	0.77	0.93
	2.5	0.61	0.85	0.50	0.82	0.77	0.91
	3.75	0.61	0.82	0.49	0.79	0.77	0.89
	4	0.62	0.79	0.51	0.76	0.77	0.88
10	1	0.76	0.90	0.54	0.84	0.87	0.96
	1.75	0.76	0.90	0.54	0.80	0.87	0.95
	2.5	0.75	0.89	0.53	0.78	0.86	0.94
	3.25	0.75	0.87	0.52	0.75	0.86	0.93
13	1	0.81	0.92	0.55	0.76	0.89	0.96
	1.75	0.81	0.92	0.54	0.76	0.88	0.96
	2.5	0.80	0.91	0.52	0.72	0.88	0.94
	3.25	0.80	0.90	0.52	0.70	0.88	0.94
16	1	0.85	0.89	0.56	0.58	0.90	0.95
	1.75	0.84	0.89	0.54	0.57	0.90	0.95
	2.5	0.84	0.88	0.55	0.55	0.89	0.94

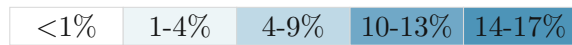


Table 4.1: NRMSA comparison of observers for sea states in tuned mode

for the three estimates compared to the linear KF. However, this is at the cost of a larger mean error, mainly due to the non-zero means in the states. In order to take into

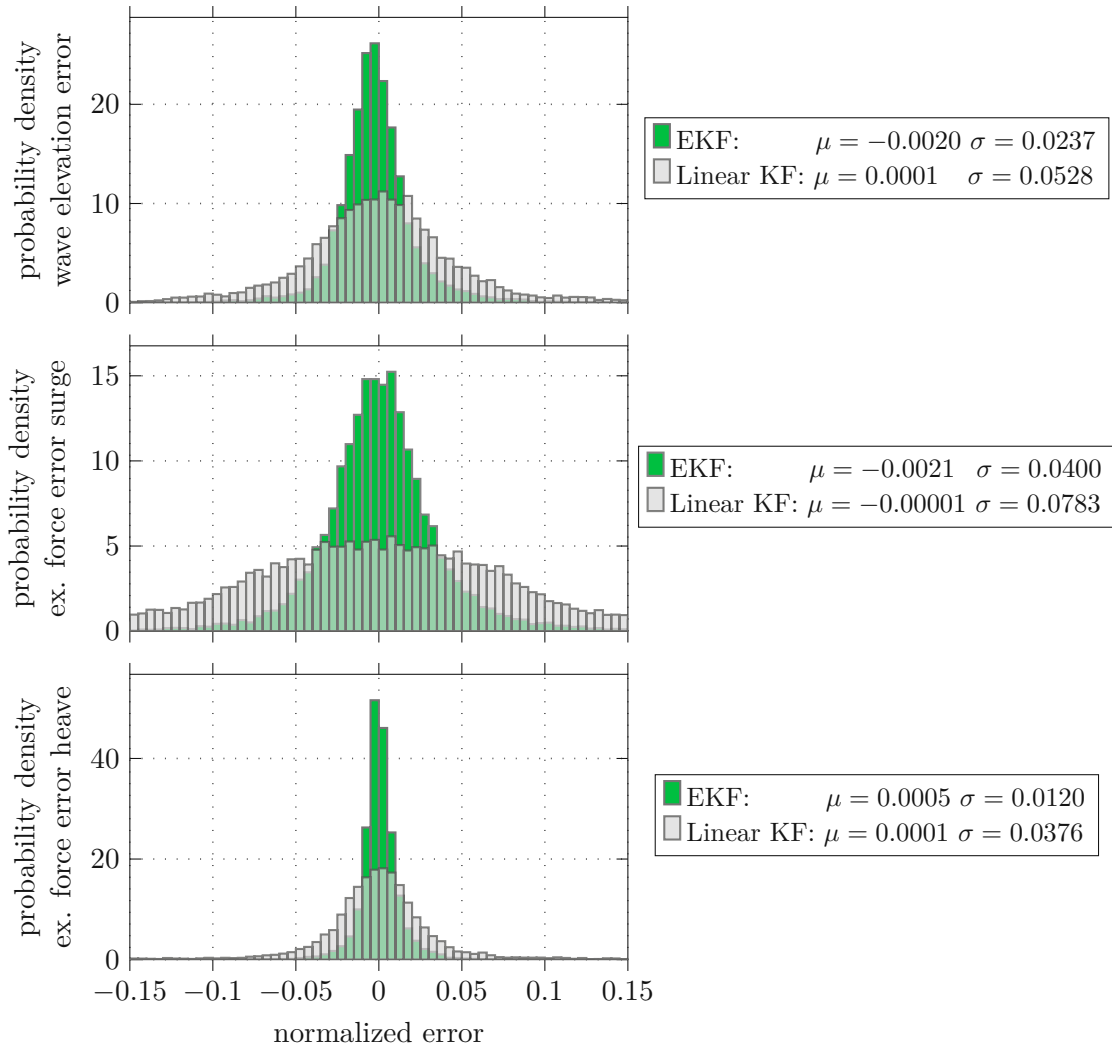


Figure 4.7: Comparison of the distribution of the estimation errors

account the minimum and maximum estimation errors into the evaluation, the observers are compared using a boxplot diagram. Figure 4.8 shows the box plots for the normalized wave elevation and excitation force errors across all sea states of the EKF and linear KF. The box corresponds to the area in which 99% of the estimation errors are located with the median indicated as line in the box. The whiskers, represented by the horizontal lines outside the box, correspond to the minimum and maximum estimation errors. As can be seen, the minimum and maximum estimation errors for the wave elevation and excitation force in heave are visibly reduced for the EKF, but not for the excitation force in surge. The reason for this is mainly due to the sea states with $T_e = 16s$ where the accuracy of the EKF decreases significantly for the excitation force estimation in surge (see Table 4.1).

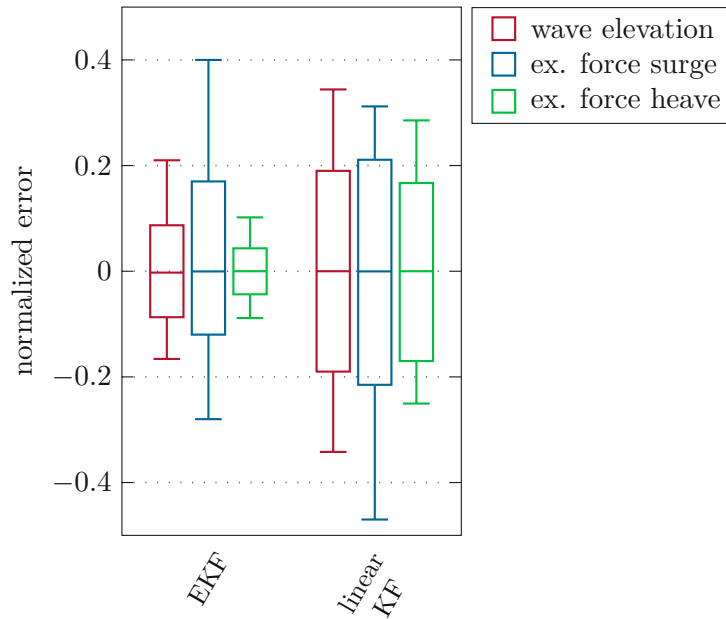


Figure 4.8: Boxplot comparison of the accuracy of the linear KF and the EKF

4.4.3 Robustness against Sensor Failures

One major limitation of the linear KF is the case of a pressure sensor failure, where no estimation of the wave elevation and consequently the excitation force in surge and heave is possible. In contrast, the EKF combines several sensors for the estimation process, allowing to assess its robustness and quality of the estimation in case of single and multiple sensor failures. For this analysis, sensor failures are simply simulated by neglecting the corresponding measurements in the output vector of the EKF. The robustness of the estimation is again determined using box plots diagrams of the normalized estimation errors across all sea states in tuned mode. Figure 4.9 shows the box plots for the wave elevation and excitation force in surge and heave of the EKF with respect to single sensor failures. Recall that the box corresponds to the area in which 99% of the estimation errors are located and the whiskers represent the minimum and maximum estimation errors. The most interesting case is probably that of a pressure sensor failure. Figure 4.9 demonstrates a notable increase in the wave elevation and excitation force error in heave, which emphasizes the relevance of the pressure sensor. When comparing the boxplots in this case with those of the linear KF in Figure 4.8, it is evident that the range where 99% of the error is concentrated is slightly smaller for the EKF (less than 20% error) than for the linear KF. However, the minimum and maximum errors are larger. It should be recalled, though, that in this case, the linear KF would not be able to provide any estimates. When examining the three remaining single sensor failures in Figure 4.9, it is apparent that the EKF remains robust against these errors. This is expected in the case of IMU errors, given the redundancy in the measurements. However, in some cases of sensor failures, the estimation of the excitation force in the surge seems to improve.

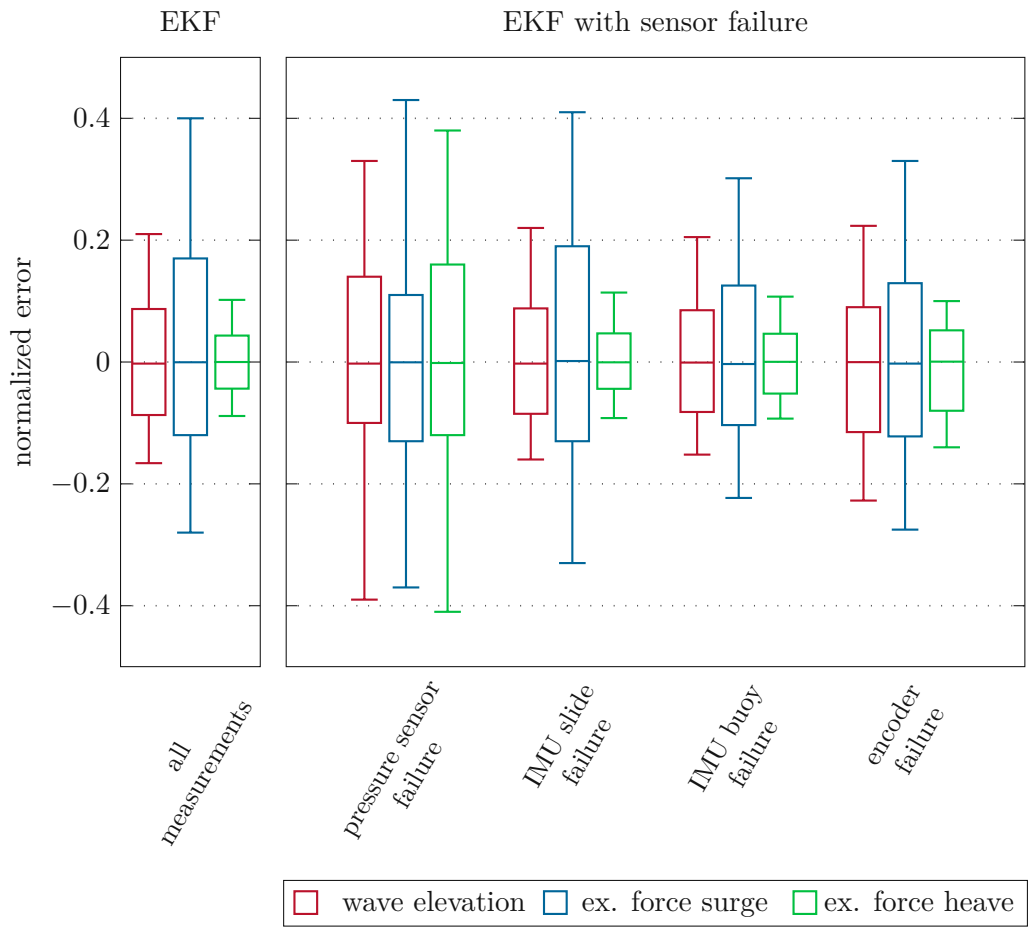


Figure 4.9: Robustness of EKF against single sensor failures

This effect could be attributed to changes in the weighting of measurements in the EKF, influenced by the entries in the covariance matrix of the measurement noise. Figure 4.10 shows further box plots for selected multiple sensor failures. As can be seen, the EKF provides reasonable results in the first two cases of sensor failures. Only in the event of a pressure sensor failure in combination with an IMU failure, there is a noticeable increase in the estimation errors. Nevertheless, 99% of the estimation errors in these cases are distributed in the range of 20% percent of the normalized error, which is again comparable to the values of the linear KF (see Figure 4.8).

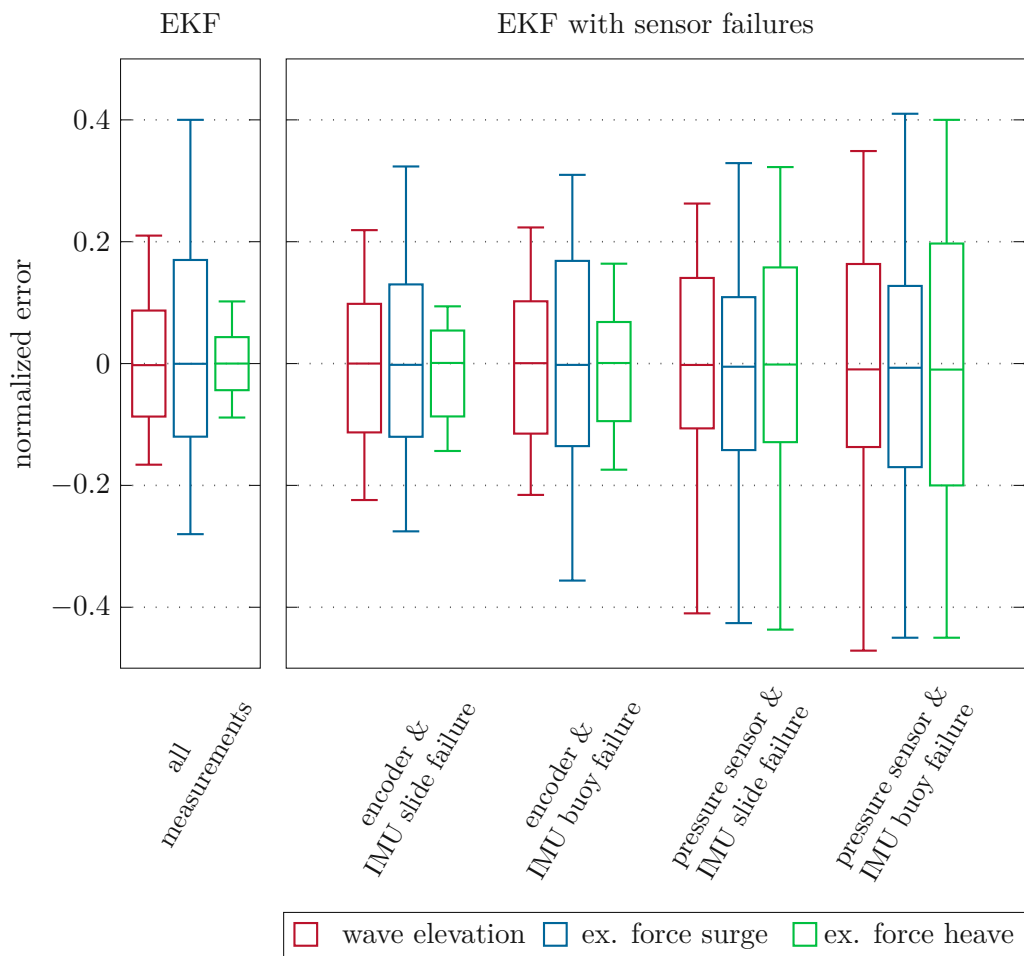


Figure 4.10: Robustness of EKF against multiple sensor failures

4.4.4 Impact of Degrees of Freedom

The estimation of the EKF is based on the 3DoF model derived in Section 3.1. To confirm the legitimacy of the 3DoF model, the estimation was also performed using an EKF based on a 1DoF model that considers only the rack position s_{rack} and a 2DoF model that considers the rack position and the pitch angle s_{rack} and θ , respectively. To investigate

the impact of the considered degrees of freedom on the estimation, the errors are plotted alongside the inclination angle. The inclination angle ψ characterizes the angle that the WEC encloses with the z -axis of the inertial frame and calculates to

$$\psi = \arccos(\cos(\varphi) \cos(\theta)). \quad (4.26)$$

Figure 4.11 shows the time series for the estimation error of the wave elevation of the EKFs depending on the degrees of freedom considered, and the inclination angle. The estimation

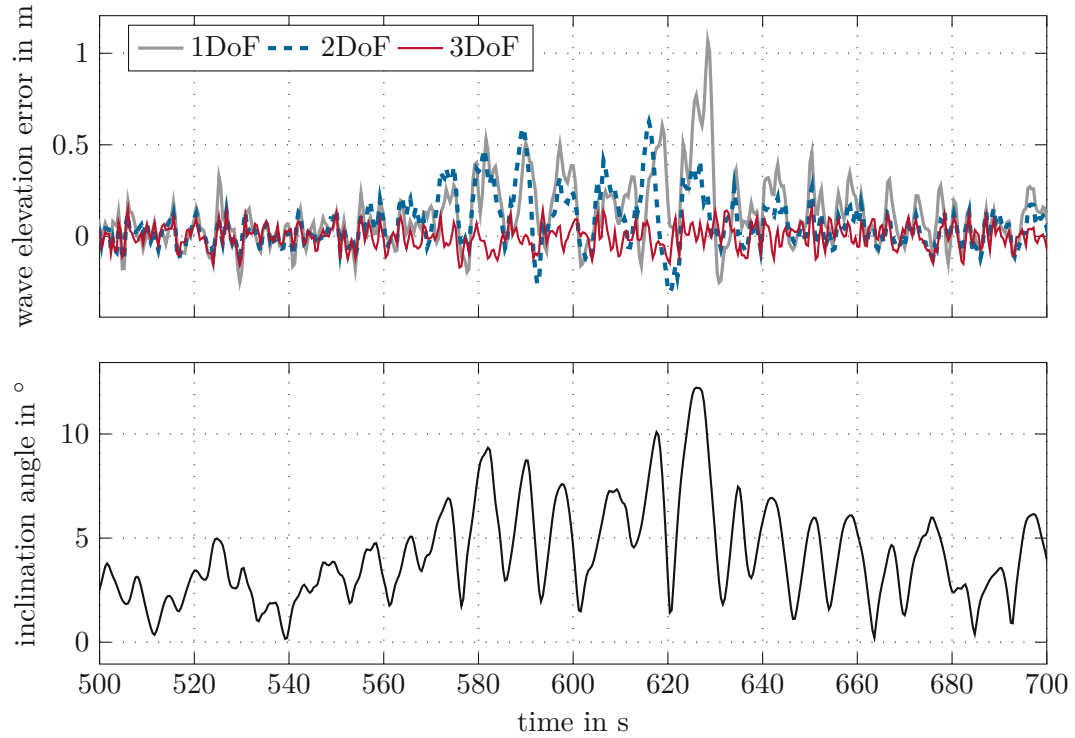


Figure 4.11: Impact of degrees of freedom considered in estimation ($H_s = 1.75\text{m}$, $T_e = 7\text{s}$).

error of the EKF based on 1DoF shows a clear correlation with the inclination angle as neither the roll nor pitch angle are considered in the model. On the other hand, the estimation error of the EKF based on 3DoFs remains unaffected by the lateral deflection of the WEC. With the 2DoF EKF, the estimation error is just slightly reduced compared to the 1DoF EKF. According to Figure 4.11, the incorporation of the roll and pitch angle into the model shows a decisive advantage with regard to the estimation error. This shows the significance of using a 3DoF model for estimation.

As already discussed in detail, the 3DoF EKF offers a significant advantage over the linear KF in terms of estimation accuracy. However, the EKF is associated with a higher computational effort, which is another crucial factor to consider when selecting a suitable algorithm for the estimation task. Simulations indicate that the computational effort for the EKF increases by a factor of approximately 50 compared to the linear KF. Despite this significant difference in complexity, an online implementation should still be feasible.

5 Conclusion and Outlook

In this work, an estimation strategy for a point absorber WEC was developed that is capable of estimating the wave elevation and the excitation force in the surge and heave direction. An EKF based on a non-linear but simplified dynamic model of the WEC was used. The model was verified using a comprehensive 6DoF W2W model showing that the simplified model is capable of capturing the relevant movements of the WEC within three degrees of freedom. As the simplified model is able to account for non-linearities due to the variable submergence of the buoy, the model could be coupled with an oscillator model for the wave elevation, which also approximates the dynamics of the excitation force in the surge and heave directions. In order to obtain reliable estimates, multiple and redundant sensors were included in the estimation process. The performance of the EKF was evaluated using W2W simulations for various sea states. A comparison between the EKF and the linear KF shows that the EKF provides better results in terms of estimation accuracy, especially for sea states with a high probability of occurrence. However, for some sea states with a lower probability of occurrence, the estimation accuracy of the EKF decreases significantly. This is particularly apparent in the estimation of the excitation force in surge. Further investigations are necessary to examine the underlying causes in more detail. In addition, the robustness of the EKF was demonstrated by simulating different sensor failures. In the case of pressure sensor failures, the accuracy of the estimate is most affected. Yet, the EKF is able to provide reliable estimates under various sensor failures. Although the predominant motion of the WEC is the heave motion, an EKF relying on a 3DoF model was shown to be crucial for obtaining accurate estimation results. Despite the improved estimation accuracy of the EKF compared to the linear KF, the impact of these results on the prediction algorithms and consequently on the power output remains to be investigated.

With regard to the results, it should be noted once again that only unidirectional waves traveling in positive surge direction were considered in the evaluation. As the EKF design only considers excitation forces in surge and heave, the results represent a best-case scenario. Future work could, for example, focus on including a parameter for a mean wave direction to account for an excitation force in the sway direction. An attempt could then also be made to estimate this parameter within the EKF. Consequently, it would be interesting to investigate the performance of the EKF under different scenarios for unidirectional and multidirectional wave conditions. In addition, the dynamic system used in the EKF has a high model order due to the oscillator model. Future work could therefore also focus on the proper choice of oscillator frequencies to reduce the computational complexity of the EKF.

Bibliography

- [1] A. Falcão, “Wave energy utilization: A review of the technologies,” *Renewable and Sustainable Energy Reviews*, vol. 14, pp. 899–918, 2010. DOI: 10.1016/j.rser.2009.11.003.
- [2] F. Mwasilu and J. W. Jung, “Potential for power generation from ocean wave renewable energy source: A comprehensive review on state-of-the-art technology and future prospects,” *IET Renewable Power Generation*, vol. 13, pp. 363–375, 2019. DOI: 10.1049/iet-rpg.2018.5456.
- [3] J. V. Ringwood, G. Bacelli, and F. Fusco, “Energy-maximizing control of wave-energy converters: The development of control system technology to optimize their operation,” *IEEE Control Systems*, vol. 34, pp. 30–55, 2014. DOI: 10.1109/MCS.2014.2333253.
- [4] CorPower Ocean, *Technology*, <https://corpowersocean.com/wave-energy-technology/>, Accessed: 2023-11-21.
- [5] J. H. Todalshaug *et al.*, “Tank testing of an inherently phase-controlled wave energy converter,” *International Journal of Marine Energy*, vol. 15, pp. 68–84, 2016. DOI: 10.1016/j.ijome.2016.04.007.
- [6] A. Pecher and J. Kofoed, *Handbook of Ocean Wave Energy*, 1st ed. Springer Cham, 2017. DOI: 10.1007/978-3-319-39889-1.
- [7] CorPower Ocean, *Brand Assets*, <https://company-230277.frontify.com/d/R8YsMrfLrpiK/brand-assets?#/media-press/media-press-kit>, Accessed: 2023-11-21.
- [8] N. Faedo, S. Olaya, and J. V. Ringwood, “Optimal control, mpc and mpc-like algorithms for wave energy systems: An overview,” *IFAC Journal of Systems and Control*, vol. 1, pp. 37–56, 2017. DOI: <https://doi.org/10.1016/j.ifacsc.2017.07.001>.
- [9] B. Guo, R. J. Patton, S. Jin, and R. Patton, “Identification and validation of excitation force for a heaving point absorber wave energy convertor,” in *Proceedings of the European Wave and Tidal Energy Conference*, Cork, IRE, Sep. 2017, pp. 1–9. [Online]. Available: <https://www.researchgate.net/publication/319261369>.
- [10] B. Guo, R. J. Patton, S. Jin, and J. Lan, “Numerical and experimental studies of excitation force approximation for wave energy conversion,” *Renewable Energy*, vol. 125, pp. 877–889, 2018. DOI: 10.1016/j.renene.2018.03.007.
- [11] A. Merigaud and J. V. Ringwood, “Incorporating ocean wave spectrum information in short-term free-surface elevation forecasting,” *IEEE Journal of Oceanic Engineering*, vol. 44, pp. 401–414, 2019. DOI: 10.1109/JOE.2018.2822498.

- [12] B. A. Ling and B. A. Batten, "Real time estimation and prediction of wave excitation forces on a heaving body," in *Proceedings of the ASME 2015 34th International Conference on Ocean, Offshore and Arctic Engineering*, St. John's, CA, May 2015, V009T09A017. DOI: 10.1115/OMAE2015-41087.
- [13] M. Garcia-Abril, F. Paparella, and J. Ringwood, "Excitation force estimation and forecasting for wave energy applications," *IFAC-PapersOnLine*, vol. 50, pp. 14 692–14 697, 2017. DOI: 10.1016/j.ifacol.2017.08.2499.
- [14] H. N. Nguyen and P. Tona, "Wave excitation force estimation for wave energy converters of the point-absorber type," *IEEE Transactions on Control Systems Technology*, vol. 26, pp. 2173–2181, 2018. DOI: 10.1109/TCST.2017.2747508.
- [15] Y. Pena-Sanchez, C. Windt, J. Davidson, and J. V. Ringwood, "A critical comparison of excitation force estimators for wave-energy devices," *IEEE Transactions on Control Systems Technology*, vol. 28, pp. 2263–2275, 2020. DOI: 10.1109/TCST.2019.2939092.
- [16] G. Bacelli and R. Coe, "State estimation for wave energy converters," Sandia National Laboratories (SNL), Tech. Rep., 2017. DOI: 10.2172/1365524.
- [17] M. Abdelrahman and R. Patton, "Robust control of a wave energy converter with soft sensing of wave excitation force," in *Proceedings of the European Wave and Tidal Energy Conference*, Cork, IRE, Sep. 2017, pp. 974-1–974-10. [Online]. Available: <https://www.researchgate.net/publication/319514368>.
- [18] M. Abdelrahman and R. Patton, "Observer-based unknown input estimator of wave excitation force for a wave energy converter," *IEEE Transactions on Control Systems Technology*, vol. 28, pp. 2665–2672, 2020. DOI: 10.1109/TCST.2019.2944329.
- [19] M. A. Bhinder, A. Babarit, L. Gentaz, and P. Ferrant, "Potential time domain model with viscous correction and cfd analysis of a generic surging floating wave energy converter," *International Journal of Marine Energy*, vol. 10, pp. 70–96, 2015. DOI: 10.1016/j.ijome.2015.01.005.
- [20] A. F. Davis and B. C. Fabien, "Wave excitation force estimation of wave energy floats using extended kalman filters," *Ocean Engineering*, vol. 198, p. 106 970, 2020. DOI: 10.1016/j.oceaneng.2020.106970.
- [21] O. Abdelkhalik, S. Zou, R. Robinett, G. Bacelli, and D. Wilson, "Estimation of excitation forces for wave energy converters control using pressure measurements," *International Journal of Control*, vol. 90, pp. 1793–1805, 2017. DOI: 10.1080/00207179.2016.1222555.
- [22] B. A. Ling, "Real-time estimation and prediction of wave excitation forces for wave energy control applications," M.S. thesis, Oregon State University, 2015.
- [23] M. Bonfanti *et al.*, "Real-time wave excitation forces estimation: An application on the iswec device," *Journal of Marine Science and Engineering*, vol. 8, pp. 1–30, 2020. DOI: 10.3390/jmse8100825.

- [24] S. Zou and O. Abdelkhalik, “Time-varying linear quadratic gaussian optimal control for three-degree-of-freedom wave energy converters,” *Renewable Energy*, vol. 149, pp. 217–225, 2020. DOI: 10.1016/j.renene.2019.12.054.
- [25] H. N. Nguyen, P. Tona, A. Mériçaud, M. Cocho, and A. Pichard, “Wave excitation force estimation for a multi-dof wec via a cubature kalman filter: Design and preliminary results,” in *Proceedings of the International Conference on Offshore Mechanics and Arctic Engineering - OMAE*, vol. 9, Virtual, Online, Jun. 2021, V009T09A016. DOI: 10.1115/OMAE2021-64189.
- [26] I. Arasaratnam and S. Haykin, “Cubature kalman filters,” *IEEE Transactions on Automatic Control*, vol. 54, pp. 1254–1269, 2009. DOI: 10.1109/TAC.2009.2019800.
- [27] A. Merigaud, J.-C. Gilloteaux, and J. V. Ringwood, “A nonlinear extension for linear boundary element methods in wave energy device modelling,” in *Proceedings of the International Conference on Offshore Mechanics and Arctic Engineering - OMAE*, Rio de Janeiro, BR, Jul. 2012, pp. 615–621. DOI: 10.1115/OMAE2012-83581.
- [28] M. Guérinel, M. Alves, and A. Sarmento, “Nonlinear modelling of the dynamics of a free floating body,” in *Proceedings of the European Wave and Tidal Energy Conference*, Southampton, UK, Sep. 2011. [Online]. Available: <https://www.researchgate.net/publication/294580110>.
- [29] G. Giorgi, M. Penalba, and J. V. Ringwood, “Nonlinear hydrodynamic models for heaving buoy wave energy converters,” in *Proceedings of AWTEC Asian Wave and Tidal Energy Conference*, Singapore, SG, Oct. 2016, pp. 1–10. [Online]. Available: <https://www.researchgate.net/publication/315714280>.
- [30] B. Méhauté, *An Introduction to Hydrodynamics and Water Waves*. Springer Berlin Heidelberg, 1976. DOI: 10.1007/978-3-642-85567-2.
- [31] T. Hedges, “Regions of validity of analytical wave theories,” *Proceedings of the Institution of Civil Engineers - Water, Maritime and Energy*, vol. 112, pp. 111–114, Jun. 1995. DOI: 10.1680/iwtme.1995.27656.
- [32] L. H. Holthuijsen, “Linear wave theory (oceanic waters),” in *Waves in Oceanic and Coastal Waters*. Cambridge University Press, 2007, pp. 106–144. DOI: 10.1017/CB09780511618536.
- [33] U. A. Korde and J. Ringwood, “Nature of the wave input,” in *Hydrodynamic Control of Wave Energy Devices*. Cambridge University Press, 2016, pp. 91–112. DOI: 10.1017/CB09781139942072.
- [34] L. H. Holthuijsen, “Description of ocean waves,” in *Waves in Oceanic and Coastal Waters*. Cambridge University Press, 2007, pp. 24–55. DOI: 10.1017/CB09780511618536.
- [35] B. Ding *et al.*, “Comparison of wave-body interaction modelling methods for the study of reactively controlled point absorber wave energy converter,” in *Proceedings of the 34th International Workshop on Water Waves and Floating Bodies (IWWWFB)*, Newcastle, AU, Apr. 2019. [Online]. Available: <https://hal.science/hal-02380033>.

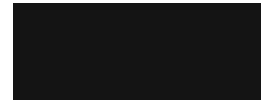
- [36] J. Falnes, “Wave-body interactions,” in *Ocean Waves and Oscillating Systems: Linear Interactions Including Wave-Energy Extraction*. Cambridge University Press, 2002, pp. 118–195. DOI: 10.1017/CB09780511754630.
- [37] *Wamit user manual version 7.4*, WAMIT, Inc., 2022.
- [38] W. Cummins, “The impulse response function and ship motions,” Department of the Navy, David Taylor Model Basin, Tech. Rep., Oct. 1962.
- [39] E. Kristiansen, Å. Hjulstad, and O. Egeland, “State-space representation of radiation forces in time-domain vessel models,” *Ocean Engineering*, vol. 32, pp. 2195–2216, 2005. DOI: 10.1016/j.oceaneng.2005.02.009.
- [40] T. Perez and T. I. Fossen, “Joint identification of infinite-frequency added mass and fluid-memory models of marine structures,” *Modeling, Identification and Control*, vol. 29, pp. 93–102, 2008. DOI: 10.4173/mic.2008.3.2.
- [41] CorPower Ocean, *An approximative method to account for instantaneous submergence in the computation of hydrodynamic forces on a floating body*, Unpublished internal company document, 2022.
- [42] J. Morison, J. Johnson, and S. Schaaf, “The force exerted by surface waves on piles,” *Journal of Petroleum Technology*, vol. 2, pp. 149–154, 1950. DOI: 10.2118/950149-G.
- [43] M. A. Bhinder, A. Babarit, L. Gentaz, and P. Ferrant, “Assessment of viscous damping via 3d-cfd modelling of a floating wave energy device,” in *Proceedings of the European Wave and Tidal Energy Conference*, Southampton, UK, Sep. 2011, pp. 5–9. DOI: 10.6084/M9.FIGSHARE.1419625.
- [44] R. Reams, “Hadamard inverses, square roots and products of almost semidefinite matrices,” *Linear Algebra and its Applications*, vol. 288, pp. 35–43, 1999. DOI: 10.1016/S0024-3795(98)10162-3.
- [45] Y. Goda, “Statistical properties and spectra of sea waves,” in *Random Seas and Design of Maritime Structures*. World Scientific Publishing Company, 2010, vol. 33, pp. 19–61. DOI: 10.1142/9789814282413_0002.
- [46] CorPower Ocean, *Scatter diagram for agucadora*, Unpublished internal company document, 2022.
- [47] A. Böge, G. Böge, W. Böge, W. Schlemmer, and W. Weißbach, *Technische Mechanik: Statik - Dynamik - Fluidmechanik - Festigkeitslehre*. Vieweg+Teubner Verlag, 2011, vol. 29. DOI: 10.1007/978-3-658-02061-3.
- [48] V. Sandberg, “Center of buoyancy definition,” Los Alamos National Laboratory (LANL), Tech. Rep., Dec. 1988. DOI: 10.2172/6687588.
- [49] B. Siciliano, L. Sciavicco, L. Villani, and G. Oriolo, *Robotics: Modelling, Planning and Control*, 1st ed. Springer Publishing Company, Incorporated, 2008. DOI: 10.1007/978-1-84628-642-1.
- [50] W. Kemmetmüller and A. Kugi, *Skriptum zur VU Modellbildung (SS 2022)*. Automation and Control Institute (ACIN), 2022.

- [51] Y. Nakayama and R. Boucher, *Introduction to fluid mechanics*, 2nd ed. Butterworth-Heinemann, 2018.
- [52] M. D. Shuster, “A survey of attitude representation,” *Journal of The Astronautical Sciences*, vol. 41, pp. 439–517, 1993.
- [53] W. Kemmetmüller and A. Kugi, *Skriptum zur VO Regelungssysteme 1 (WS 2020/2021)*. Automation and Control Institute (ACIN), 2020.
- [54] A. F. Davis and B. C. Fabien, “Systematic identification of drag coefficients for a heaving wave follower,” *Ocean Engineering*, vol. 168, pp. 1–11, 2018. DOI: 10.1016/j.oceaneng.2018.08.054.

Eidesstattliche Erklärung

Hiermit erkläre ich, dass die vorliegende Arbeit gemäß dem Code of Conduct - Regeln zur Sicherung guter wissenschaftlicher Praxis (in der aktuellen Fassung des jeweiligen Mitteilungsblattes der TU Wien), insbesondere ohne unzulässige Hilfe Dritter und ohne Benutzung anderer als der angegebenen Hilfsmittel, angefertigt wurde. Die aus anderen Quellen direkt oder indirekt übernommenen Daten und Konzepte sind unter Angabe der Quelle gekennzeichnet. Die Arbeit wurde bisher weder im In- noch im Ausland in gleicher oder in ähnlicher Form in anderen Prüfungsverfahren vorgelegt.

Wien, 2. Januar 2024



Tobias Glaser